



Research Article

Effect of texture on deformation behavior of heterogeneous Mg-13Gd alloy with strength–ductility synergy



Shuaishuai Liu^{a,b}, Han Liu^{a,b}, Xiang Chen^{a,b}, Guangsheng Huang^{a,b,*}, Qin Zou^{a,b}, Aitao Tang^{a,b}, Bin Jiang^{a,b,*}, Yuntian Zhu^{c,d}, Fusheng Pan^{a,b}

^a State Key Laboratory of Mechanical Transmission, College of Materials Science and Engineering, Chongqing University, Chongqing 400044, China

^b National Engineering Research Center for Magnesium Alloys, Chongqing University, Chongqing, 400044, China

^c Department of Materials Science and Engineering, City University of Hong Kong, Hong Kong, 999077, China

^d Nano and Heterogeneous Material Center, Nanjing University of Science and Technology, Nanjing, 210094, China

ARTICLE INFO

Article history:

Received 21 July 2021

Revised 5 September 2021

Accepted 19 September 2021

Available online 10 January 2022

Keywords:

Mg–Gd alloy

Recrystallization

Heterogeneous texture

Mechanical properties

HDI hardening

ABSTRACT

Heterostructure metals as a new class of materials can effectively break the traditional strength–ductility trade-off dilemma. In this study, the extruded sheet with the small extrusion ratio (ER) of 3.9 (ER3.9) presented a heterogeneous lamella structure (HLS) and texture, where the fine dynamical recrystallized (DRXed) grains formed a random texture and coarse un-DRXed grains exhibited a strong basal texture. The ER3.9 sample presented an excellent combination of strength and ductility. The texture strengthening in coarse grains and hetero-deformation induced (HDI) strengthening contributed to the enhanced strength of the ER3.9 sample besides grain refinement. The improving ductility mainly stems from the weakened texture in fine grains. Interestingly, in coarse grains, the strong basal texture, the occurrence of cross slip, low stacking fault energy (SFE), and dislocation pinned by precipitates weaken the HDI hardening effect. While the traditional dislocation hardening mainly generated by fine grains dominates overall strain hardening. Meanwhile, the activation of non-basal slips, especially pyramidal ($c + a$) slip, and the generation of cross slips in fine grains benefit for coordinating plastic deformation. The ability for coordinate plastic deformation in fine grains is higher than that of coarse grains, which was confirmed by the digital image correlation technology. This work will promote the development of the heterogeneous theory in textured Mg alloys.

© 2022 Published by Elsevier Ltd on behalf of The editorial office of Journal of Materials Science & Technology.

1. Introduction

High strength and ductility of metal materials have been of interest for the materials community such as automobile, aerospace, power, and building construction [1], etc. Nano/ultrafine-grain obtained by severe plastic deformation or other process methods can significantly enhance strength, but this usually comes at the expense of ductility due to dramatic loss of strain hardening. Thus, the problem of strength–ductility trade-off dilemma has been a lasting challenge for researchers.

Recently, heterostructured materials present their potential in the combination of strength and ductility [2]. It is generally de-

finer as materials consisting of micrometers to nanometers domain with significantly different strength, including laminate structure, harmonic structure, gradient structure, bimodal structure, heterogeneous lamella structure, dual-phase steel [3], etc. During the deformation of heterogeneous metallic materials, in the elastic–plastic stage, the remarkably different flow stresses between soft domain and hard domain generate remarkable strain gradient, which induces accumulation of geometrically necessary dislocations (GNDs) at the interface in soft domains to accommodate strain gradient, resulting in the generation of back stress, which makes the soft domains appear stronger [4]. In terms of physical processes, the formation of back stress also leads to the generation of forward stress in hard domains [5]. Hetero-deformation induced (HDI) stress is a combined effect of back stress and forward stress [4]. As the strain continues to increase, the soft domain will be subjected to higher plastic strain, leading to the further increase

* Corresponding authors.

E-mail addresses: gshuang@cqu.edu.cn (G. Huang), jiangbinrong@cqu.edu.cn (B. Jiang).

of strain gradient, which needs more GNDs to accommodate the increasing strain gradient, producing extra strain hardening based on traditional dislocation hardening. The observed high strength is due to HDI stress strengthening and enhanced tensile ductility can be attributed to the extra strain hardening, i.e., HDI hardening.

Magnesium (Mg) alloys as the lightest metal structure material have a wide application in the fields of aerospace, automotive, transportation, electronic 3C, biomedical, and energy sectors [6,7], etc. However, for structural materials of Mg alloys, the relatively poor ductility hampers their large-scale application due to limited activated slip systems. The heterogeneous structure provides a new strategy for us to elevate Mg alloys' strength and ductility simultaneously. Note that the studies of heterostructures mainly focus on face-centered cubic (FCC) or body-centered cubic (BCC) crystal structure, such as Cu/Cu–10 Zn [8], SUS304L steel [9], 1350 Al [10], Cu–Ag [11], and pure Ti [2], etc. The common characteristic among these heterostructures is their capability to generate HDI strengthening to improve strength and HDI hardening to maintain ductility [8]. Mg alloys often tend to form strong basal texture during plastic deformation since the hexagonal close-packed (HCP) crystal structure leads to a limited amount of slip systems, which makes them show obvious anisotropy of mechanical properties in subsequent loading. It is not clear whether the texture in heterostructured Mg alloys has a competitive or synergistic effect on HDI strengthening and hardening generated by the heterostructure. Thus, important work remains to be conducted to investigate the interaction of HDI strengthening and hardening and texture of heterostructured Mg alloys.

Among all types of reported heterogeneous materials, heterogeneous lamella structure (HLS) can be seen as a near-ideal heterogeneous structure since unprecedented higher HDI strengthening and hardening lead to superior strength and ductility [3]. Due to the limitations of current equipment, the parts or products with large cross-sections can be easily processed by a small extrusion ratio in industrial production [12]. Moreover, compared to other methods for preparing the heterogeneous structure, such as annealing after severe plastic deformation process [13,14], alloying addition [15], surface mechanical grinding treatment [16,17], etc., the traditional extrusion process with a small extrusion ratio can easily prepare the heterogeneous structure and greatly decrease the processing time and cost.

To simplify the research system and eliminate the complexity of multicomponent alloys, a binary Mg alloy can be designed to systematically study the relationship between microstructures and properties. It was reported that the Gd has obvious aging precipitation strengthening when the Gd content exceeds 10% (wt.%) [18]. In addition, the addition of Gd can also refine the grain, weaken the texture and promote the activation of non-basal slips to coordinate the strain [19]. Therefore, the binary Mg–13Gd (wt.%) alloy was selected. In this study, the binary Mg–13Gd alloy with HLS was fabricated by a small extrusion ratio of 3.9. At the same time, the coarse un-DRXed grains with strong basal texture and the fine DRXed grains with random texture formed. The difference of texture between coarse and fine grains was first described as heterogeneous texture. The evolution of heterogeneous microstructure and texture and the development of mechanical properties were revealed. The effect of heterogeneous texture on coarse and fine grains in Mg–13Gd alloy behind excellent strength–ductility synergy was studied in detail.

2. Experimental materials and methods

Fig. 1(a) shows the schematic diagram of the extrusion process for different samples. The as-cast Mg–13Gd with the actual chemical composition of Mg–12.67Gd was determined through inductively coupled plasma spectrometry, which was cut into the

cuboid blocks with the dimension of 15 mm × 15 mm × 38 mm, and then these cuboid blocks were homogenized at 500 °C for 24 h, followed by water quenching. The treated blocks called solid-solution (SS) samples were extruded into sheets with the thicknesses (ND) of 1.5 mm, 3 mm, and 5 mm and the width of 15 mm by dies for different sizing belts under the extrusion temperature of 330 °C after polishing. The cross-sectional area of the extrusion cylinder was 17 mm × 17 mm. Thus, corresponding extrusion ratios were 12.8, 6.4, and 3.9, respectively. The ED, TD, and ND shown in Fig. 1 represent the extrusion, transverse, and normal direction, respectively. The samples after extrusion are hereinafter referred to as ER12.8, ER6.4, and ER3.9 samples. Before extrusion, graphite water was sprayed on the inner wall of the extrusion container as a lubricant. During extrusion, the extrusion rate was ~6 mm/s.

The in-situ electron backscattered diffraction (EBSD) tests were performed to characterize the evolution of microstructures and texture of the ER3.9 sample at different strains. The in-situ tensile sample is dog-bone shaped with the gauge dimension of 11 mm (ED) × 1 mm (ND) × 1 mm (TD) (Fig. 1(b)) and the tensile direction is along ED. The in-situ tensile device developed by our research group is shown in Fig. 1(c) [20]. Before tests, in-situ tensile samples were mechanically polished to achieve a mirror-like surface, and subsequently electro-polished with ACII solution at –25 °C, 20 V for 120 s. In-situ EBSD tests were conducted on a JOEL JSM 7800 F field emission scanning electron microscope (SEM), using a step size of 0.5 μm. The transmission electron microscope (TEM, FEI TECNAI G2 F20) tests were performed to characterize the ER3.9 sample with 2% strain. The TEM thin foils were obtained from the ED–ND plane of the ER3.9 sample with 2% strain and fabricated by grinding and polishing to ~50 μm in thickness, and then by Ar ion milling to perforation. The uniaxial tension and loading–unloading–reloading (LUR) tests along ED were carried out on a universal testing machine (CMT6305–300KN) with a strain rate of 1×10^{-3} /s at room temperature. According to ASTM standard E2448, the dog-bone shaped tensile samples with the thicknesses (ND) of 1.5 mm, 3 mm, 5 mm were cut from the extruded sheets via wire-electrode, which had a gauge length of 18 mm (ED) × 4 mm (TD). During LUR tests, when the sample was loaded a certain displacement value at the rate of 0.75 mm/min, it was unloaded to 20 N with the same rate in a load-control mode, followed by reloading to the same applied load. The tensile and LUR tests for each sample were repeated three times to acquire reliable results.

The low- and high-resolution digital image correlation (hereafter referred to as LR-DIC and HR-DIC, respectively) technologies were used to investigate the evolution of the macroscopic and microscopic strain distribution of samples. For LR-DIC tests, the size of specimens is the same as that of samples for determining the mechanical properties. Before tests, the random speckle pattern in μm-scale was obtained by spraying black and white speck markers on the ED–TD plane of the tension samples. A CCD camera was employed to trace graphs at different strains to acquire the total strain distribution. For HR-DIC tests, the size of specimens was the same as that of in-situ tensile samples. Before the tests, the nm-scale speckle pattern on the ED–ND plane of the in-situ tensile samples was prepared by etching with FeCl₃ solution under the condition of –25 °C. To eliminate the residual surface caused by wire cutting, specimens were ground and electrochemically polished with ACII solution for –25 °C, 120 s at 20 V before etching. High magnification (1200X) SEM images were obtained with relatively low acceleration voltage (15 kV) and working distance (12 mm) at different strains to map the microscopic scale strain. The common calculated principle of strain for LR-DIC and HR-DIC is that the relative displacement of material with speckle mark before and after deformation are calculated by the relevant procedure in MatLab software.

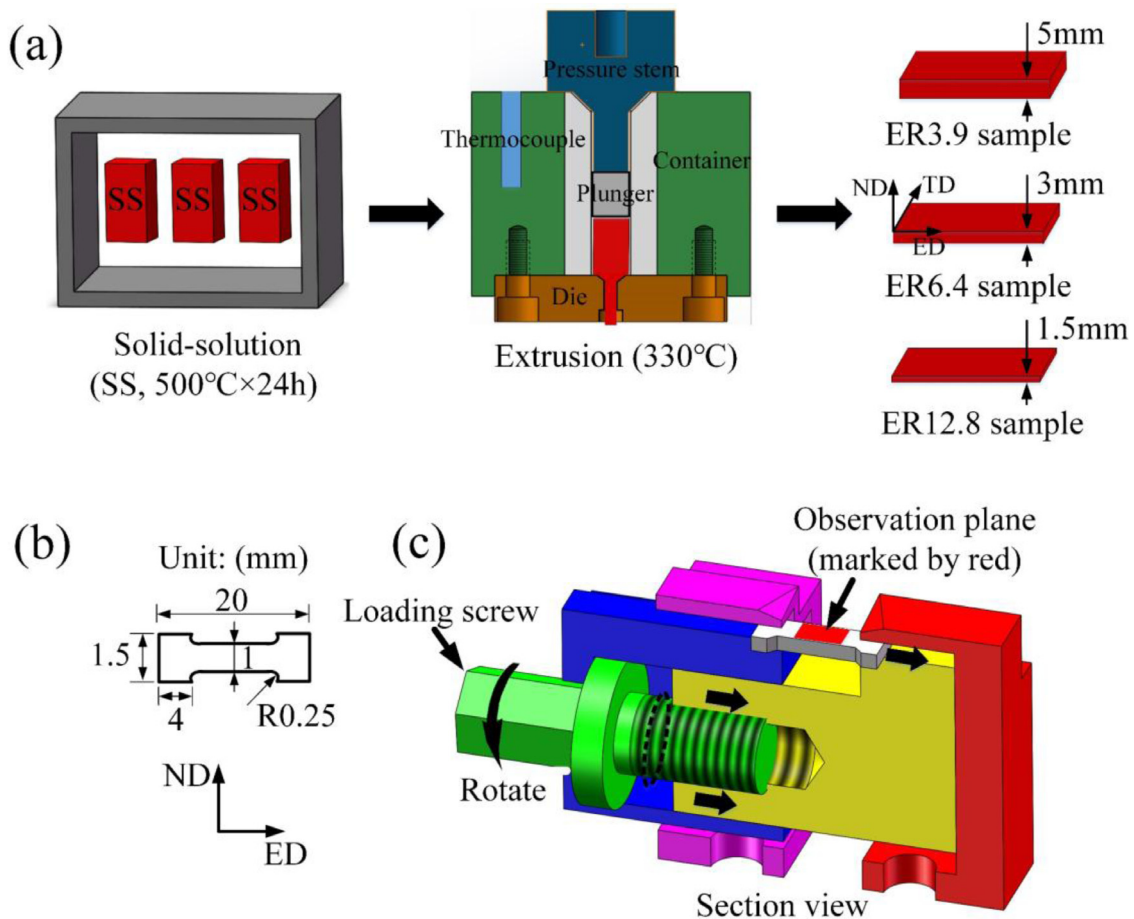


Fig. 1. (a) Schematic diagram of the extrusion process for different samples; (b) the dimension of in-situ ER3.9 tension sample and (c) schematic of the in-situ tension device [20].

3. Results

3.1. Evolution of HLS and heterogeneous texture

Compared to the sample before SS, most of the bulk precipitates in the SS sample have been dissolved, as shown in Fig. 2(a, b). The EDS results (Fig. 2(c)) demonstrate that the precipitates at points A and B marked in Fig. 2(a) are identified as Mg_5Gd or Mg_3Gd . As seen from Fig. 2(d–f), it is noticeable that the distribution of nanoscaled precipitates in the ER12.8 sample mainly focuses on the grain boundaries, while that of ER6.4 and ER3.9 samples are dispersed both at grain boundaries and inside grains. Fig. 2(g–i) shows the optical microstructures on the ED–ND planes of the samples at various extrusion ratios. It can be seen that the ER12.8 sample presents equiaxed grains, indicating that DRX has completely occurred during the hot extrusion process. Note that the ER6.4 sample appeared a few partial elongated coarse un-DRXed grains along ED. Moreover, the size of DRXed grains was smaller than that of the ER12.8 sample. As the extrusion ratio decreased to 3.9, the proportion of un-DRXed grains increased significantly and the size of DRXed grains further decreased, which well presents an HLS.

Fig. 3 shows EBSD inverse pole figure (IPF) maps on the ED–ND planes, (0001) pole figures, and histogram of the grain size distribution of the ER12.8, ER6.4, and ER3.9 samples. The ER12.8 sample with the average grain size (AGS) of $12.8 \mu m$ has a homogeneous structure and the distribution of texture component is random, exhibiting a weak texture intensity (Max = 6.78) (Fig. 3(a–

c)). While the ER6.4 sample with AGS of $7.7 \mu m$ shows a nearly homogeneous structure, which has a few partial elongated coarse un-DRXed grain (11.8%) along ED and a large number of fine DRXed grains (Fig. 3(d, f)). Due to the strong basal texture of coarse un-DRXed, the c -axes of the grains are tilted 29.4° – 63.3° from the ND towards the TD (Fig. 3(e)), which may be related to the activation of prismatic slips [21]. In addition, the extruded Mg alloys containing more than 10 wt.% Gd easily generate an extraordinarily rotated texture [19]. Herein, it should be pointed that the proportion of the coarse un-DRXed grain and the tilted angle information calculated by the Channel 5 software are based on their area fraction and maximal texture intensity in pole figures, respectively.

For the ER3.9 sample, the AGS is sharply decreased to $4.6 \mu m$ (Fig. 3(i)). Generally, the deformed alloys with a large extrusion ratio can effectively refine the grain since the larger thermal deformation activation energy promotes more DRXed grains. Note that the AGS ($12.8 \mu m$) of the ER12.8 sample is larger than that ($4.4 \mu m$) of fine grains in the ER3.9 sample. This is mainly attributed to that the driving force of DRXed grains growth in the ER12.8 sample is greater than that of ER 3.9 sample. For the ER3.9 sample, the partially recrystallized nuclei can simultaneously satisfy the condition of the thermodynamic and kinetic related to the Gibbs free energies at a small extrusion ratio [22,23]. However, the lower thermal deformation activation energy has an insufficient driving force to promote the growth of DRXed grains, while the larger thermal deformation activation energy and deformation heat in the ER12.8 sample caused by the high extrusion ratio contribute to the growth of DRXed grains during extrusion [24]. Fur-

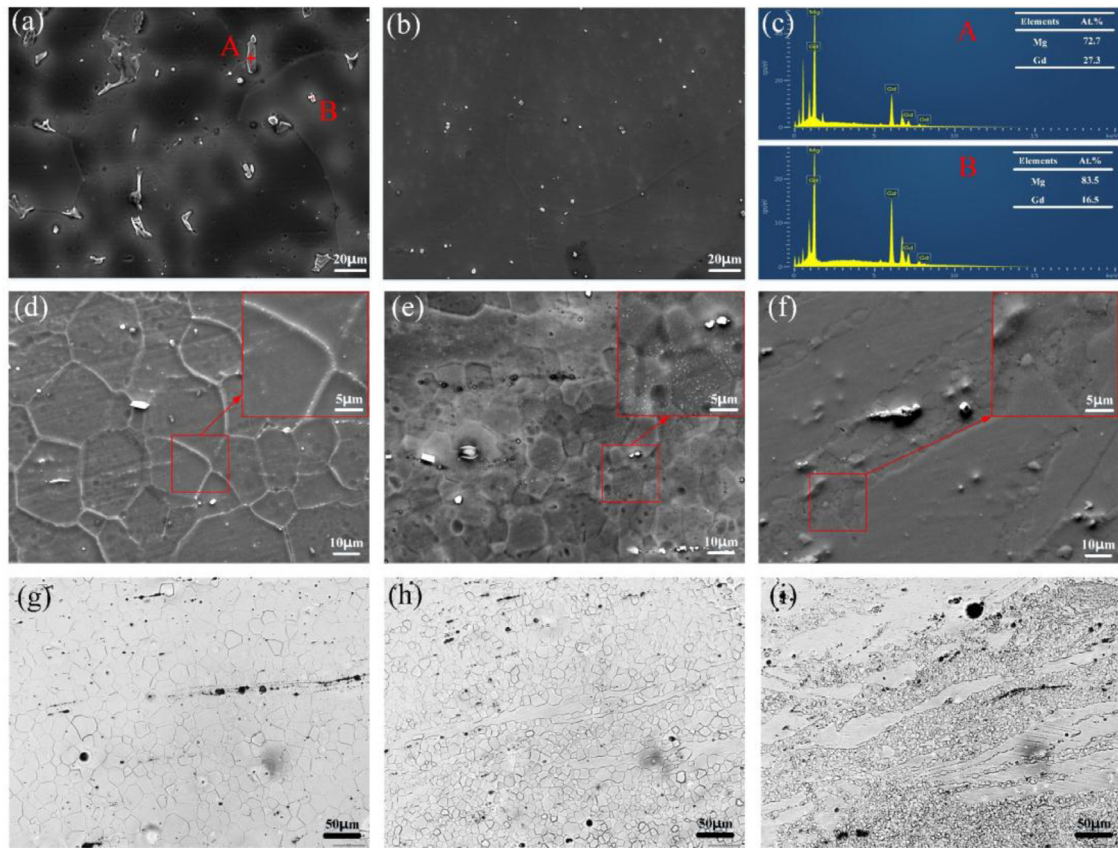


Fig. 2. SEM images of (a) the sample before SS, (b) the SS sample, and (c) EDS results of the precipitates at points A and B marked in (a); SEM images of the (d) ER12.8 sample, (e) ER6.4 sample, and (f) ER3.9 sample; optical micrographs of the (g) ER12.8 sample; (h) ER6.4 sample and (i) ER3.9 sample.

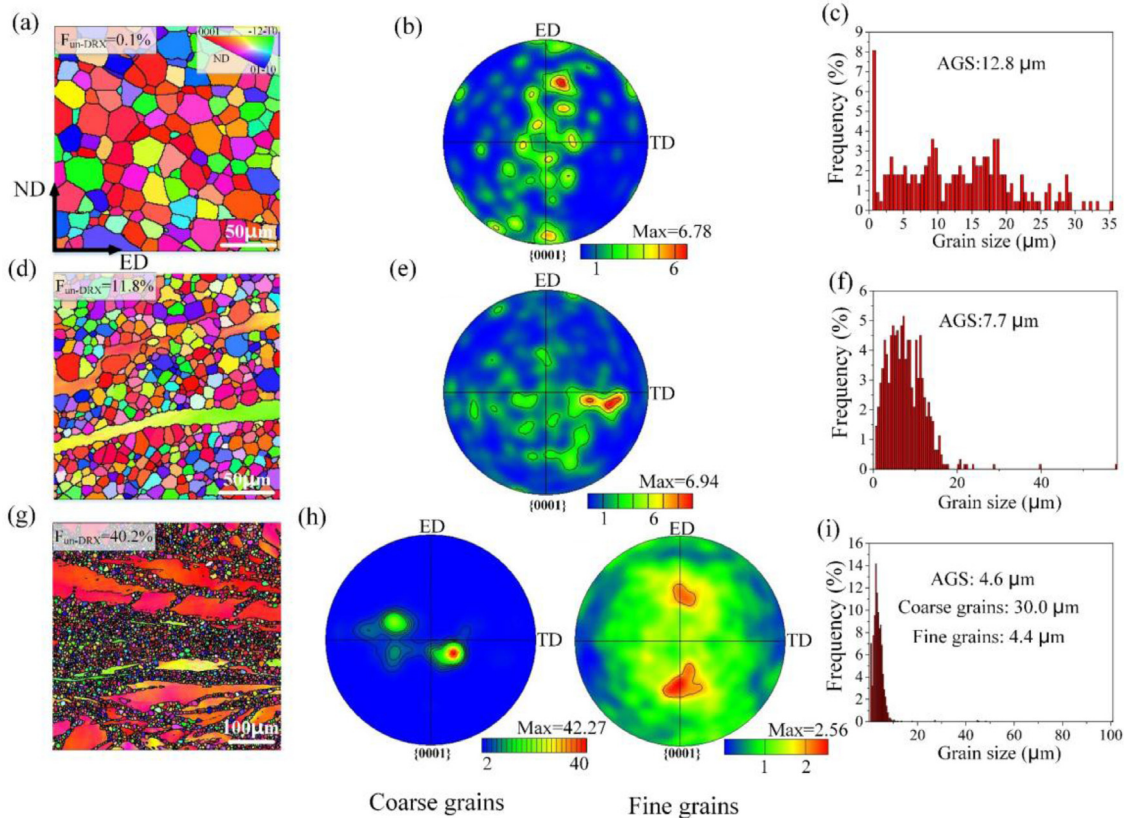


Fig. 3. EBSD inverse pole figure (IPF) maps, (0001) pole figures, and corresponding grain size distributions: (a)–(c) ER12.8 sample, (d)–(f) ER6.4 sample, and (g)–(i) ER3.9 sample.

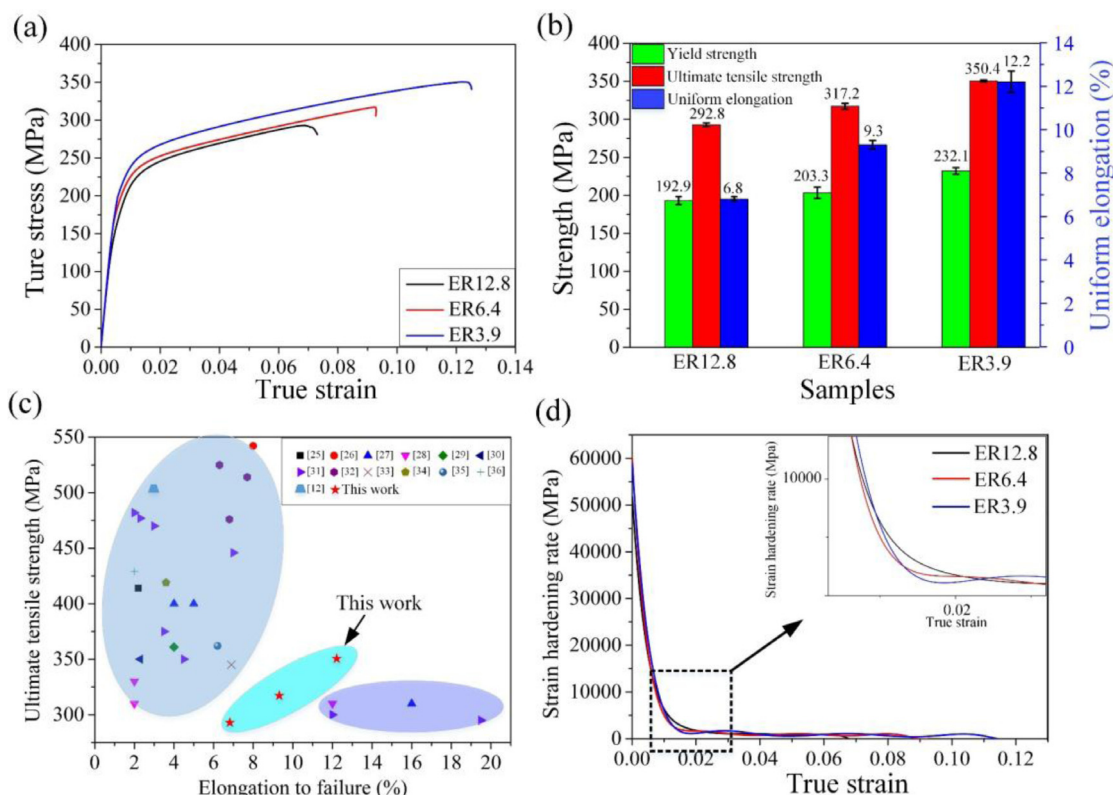


Fig. 4. (a) Tensile true stress–true strain curves of the ER12.8, ER6.4, and ER3.9 samples; (b) development of tensile properties for various samples; (c) a comparison of strength and ductility between the present work and other extruded Mg alloys containing RE [12,25–36]; (d) strain hardening rate as a function of true strain for various samples and the corresponding close-up view of the up-turns marked by a dotted box.

thermore, the proportion of coarse un-DRXed grains increases to 40.2%, and the DRXed grains are further refined, which exhibits a typical HLS (Fig. 3(g)). The *c*-axes of fine DRXed grains deflected different angles from ND to the ED and TD, consequently inducing relatively weaker texture intensity (Max = 2.56), which was similar to the ER12.8 sample. Meanwhile, the bimodal texture along ED was also generated. However, the {0001} basal planes in the coarse un-DRXed grains are nearly parallel to the ED, presenting a strong basal texture (Max = 42.27) (Fig. 3(h)). This remarkable difference of texture component between coarse and fine grains is called heterogeneous texture.

3.2. Mechanical property

Tensile true stress–true strain curves and the development of tensile properties of ER12.8, ER6.4, and ER3.9 samples are shown in Fig. 4(a, b), respectively. Apparently, with decreasing extrusion ratios, the yield strength (YS), the ultimate tensile strength (UTS), and the elongation (EI) gradually increase. The ER3.9 sample had an optimal combination of YS (232.1 MPa), UTS (350.4 MPa), and EI (12.2%), which corresponding increased by 16.9%, 20.3%, and 79.4% compared to the ER12.8 sample with the homogeneous structure. To present the advantages of excellent strength–ductility synergy fabricated by small extrusion ratio, we compared this work with other extruded Mg alloys containing rare elements (RE), which were previously reported in the literature [12,25–36]. As displayed in Fig. 4(c), the mechanical properties in previous studies show a strength–ductility trade-off. The ER3.9 sample with heterogeneous structure can effectively obtain excellent strength–ductility synergy.

The strain hardening rate ($\theta = d\sigma/d\varepsilon$) of the ER3.9 sample shows a dramatic up-turn near the 2% strain marked by the rect-

angle dotted box and maintains a larger plastic strain near fracture (Fig. 4(d)). This demonstrates that the ER3.9 sample possesses extra strain hardening, which is similar to the HLS structure including IF steel [37], Fe₂₀Co₂₀Ni₄₁Al₁₉ [38], Cu-30 Zn [4], etc. The common physics that links these extra strain hardening is the evident mechanical incompatibility between the coarse and fine grains due to the difference of dislocation storage ability. During the elastic–plastic transition period, the change of stress state near domain boundary will induce the activation of more dislocations to coordinate the mechanical incompatibility, resulting in the observed extra strain hardening [37,39,40].

3.3. Fracture morphology

Fig. 5 shows the SEM morphologies of the fracture for ER12.8, ER6.4, and ER3.9 samples at various magnifications. As seen from low magnification (Fig. 5(a–c)), the sizes of the dimples gradually decrease with the decreasing extrusion ratios. Moreover, the fine- and coarse-grain regions of the fracture in the ER3.9 sample can be easily distinguished. It is observed from high magnification (Fig. 5(d–e)) that the ER12.8 sample with larger AGS exists amounts of brittle fracture regions and cleavage planes, showing a characteristic of brittle fracture. The precipitates were also observed at the bottoms of the dimples in the ER6.4 sample. Compared to the ER6.4 sample, the number of dimples in the ER3.9 sample further increased. Unlike ER12.8 and ER6.4 samples, the coarse and fine grains of the ER3.9 sample presented two fracture morphologies, where the coarse grains distributed at some cleavage planes and brittle fracture regions, and fine grains presented amounts of small and shallow dimples marked by white arrows. These results are consistent with the deformation behavior of coarse and fine grains in the ER3.9 sample discussed below.

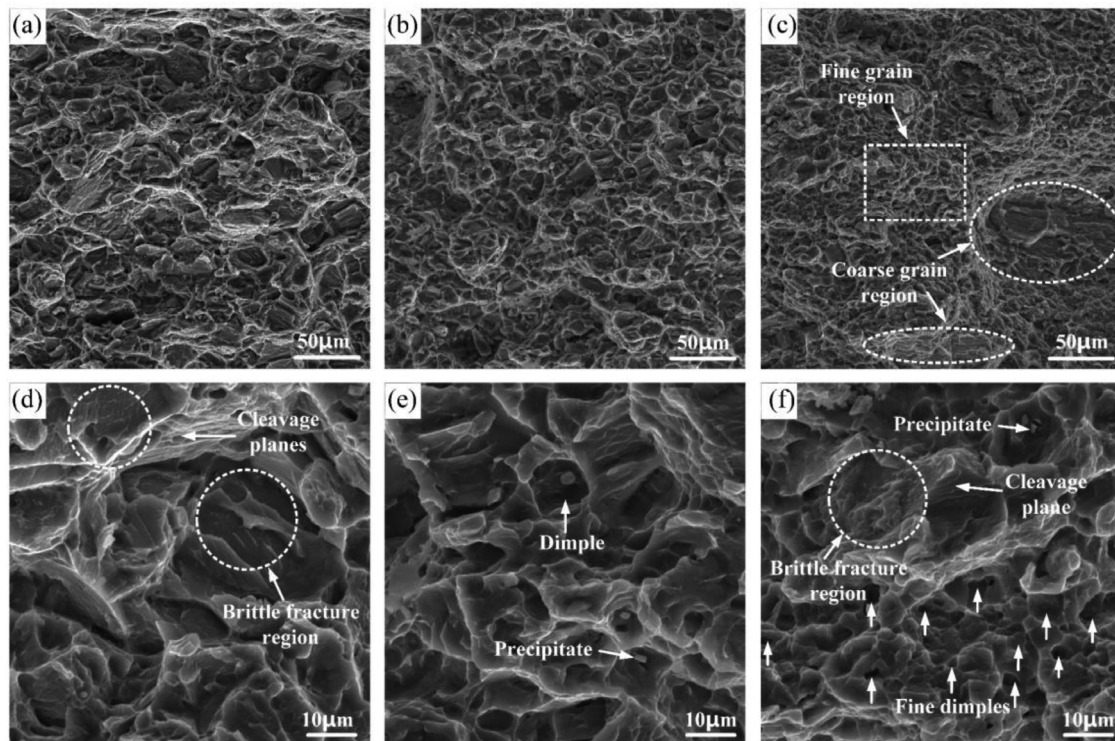


Fig. 5. SEM morphology of the fracture after tensile tests for (a) and (d) ER12.8 sample, (b) and (e) ER6.4 sample, and (c) and (f) ER3.9 sample.

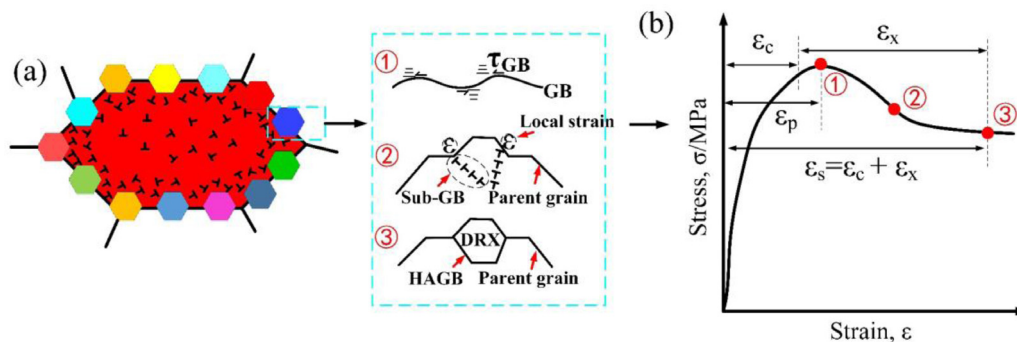


Fig. 6. (a) Schematic diagram of the nucleation of DRX grain; (b) corresponding hot working stress-strain curve.

4. Discussion

4.1. Formation mechanism of heterogeneous microstructure and texture

Fig. 6(a) presents the schematic diagram of the nucleation of the DRXed grain. These DRXed grains distributed around the parent grain show a necklace structure as typical discontinue DRX (DDR), where the sites for nucleation occur preferentially at grain boundaries (GBs) due to the low recrystallization kinetics and fewer nucleation sites in the parent grain [41–43]. During the nucleation of DRXed grain, due to the incompatibilities between parent and DRXed grains, the boundary shape is fluctuated, which hampers further grain sliding or shearing, resulting in local strain concentration near the boundary of parent grain [44]. Meanwhile, dislocations with high density accumulate at the boundary of parent grain to accommodate the plastic strain, resulting in the formation of Sub-GB (i.e., low angle grain boundaries (LAGBs)), and further, the sub-grains generates. Subsequently, the newly generated GB of DRXed grain eventually forms since the surrounding dislocations are absorbed by LAGBs continuously, then turns into high

angle grain boundaries (HAGBs) [45]. Due to the relatively lower plastic deformation under a small extrusion ratio, the thermal deformation activation energy is smaller, resulting in lower dynamic recrystallization driving force and recrystallization degree and thus the formation of heterogeneous microstructure, which is frequently observed in Mg-13Gd-4Y-2Zn-0.5Zr alloy [46], AZ91 alloy [47] and Al alloy [48].

Herein, it should be proposed that the DDRX process exists work hardening generated by the formation of constant dislocations during plastic deformation and dynamic recovery (DRV) reflected by dislocation annihilation [45], confirming the assumption in Section 4.2. The two mechanisms compete with each other and can be expressed by the following Eq. (1):

$$d\rho/d\varepsilon = d\rho^+/d\varepsilon + d\rho^-/d\varepsilon \quad (1)$$

where ρ is the dislocation density and ε is the strain. If the rate of dislocation annihilation in DRV is lower than that of work hardening, a critical DDRX condition will reach the critical dislocation density (ρ_c) [49]. The critical condition can be obtained by Eq. (2):

$$\varepsilon_c = A\varepsilon_p \quad (2)$$

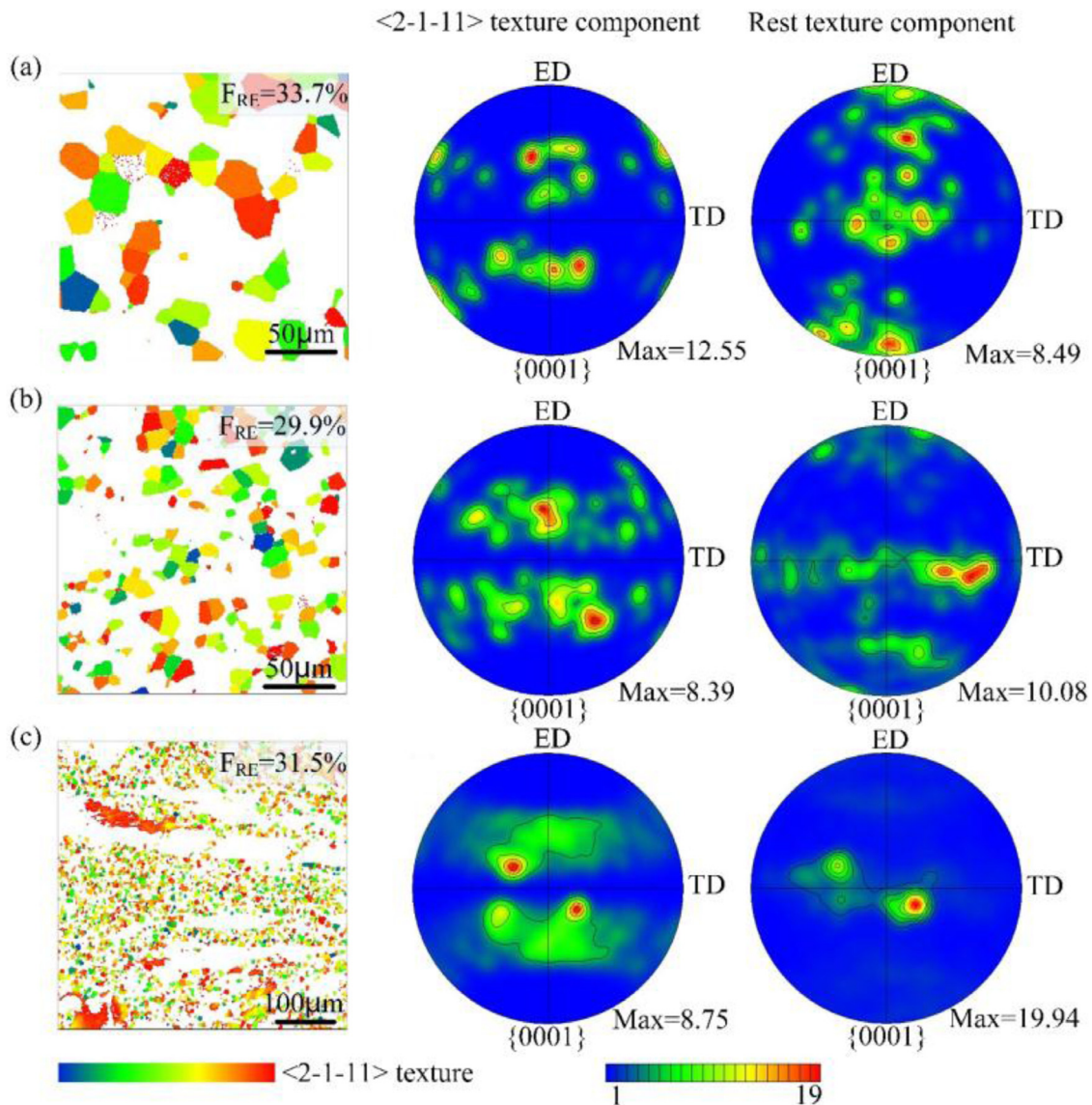


Fig. 7. Rare earth texture and rest texture component: (a) ER12.8 sample, (b) ER6.4 sample, and (c) ER3.9 sample.

where ε_c and ε_p represent the critical strain and the peak strain occurring DDRX, respectively. A is a material constant (0.2–0.8) depending on the properties of the material [50,51]. Generally, ε_c is used as the criterion for the critical condition instead of ρ_c . This is because ε_c related to ε_p can be obtained easily by the flow stress curve [45]. This also can be reflected by Fig. 6(b), where ε_x and ε_s represent the strain for one DDRX-cycle and steady-state, respectively. Therefore, based on a critical DDRX condition with ρ_c in Eq. (1), ε_c in Eq. (2) provides a theoretical criterion for us to design the heterogeneous structure with different ratios of coarse and fine grains without considering the texture.

Unlike basal fiber texture of RE-free extruded Mg alloys, the RE texture is usually present in extruded Mg-RE alloys. The RE texture $\langle 2\bar{1}\bar{1}1 \rangle$ component with rainbow dyeing scheme is shown in Fig. 7(a–c). Note that the $\langle 2\bar{1}\bar{1}1 \rangle$ texture components in three samples with different extrusion ratios nearly remain at a similar percentage, and they mainly exist in the DRXed grains. The $\{0001\}$ pole figure indicates that $\langle 2\bar{1}\bar{1}1 \rangle$ texture leads to the bimodal texture along ED in three samples, which may be attributed to shear band formation, grain boundary pinning of Mg-RE precipitates, non-basal slip activation, and the solute drag effect [19]. In

addition, their bimodal texture gradually deflects towards TD with the decrease of extrusion ratio. While rest texture components of ER6.4 and ER3.9 samples exhibit a deflection of basal poles toward TD due to the coarse un-DRXed grains. Among these rest components, the fine DRXed grains are evolved from large misorientation gradients, leading to the different orientations among them. During the extrusion process, these fine DRXed grains may rotate from their original orientations, which further makes the (sub) boundary misorientations of neighboring grains increase [52]. However, the coarse parent grains with un-DRX still retain original orientations due to lower recrystallization kinetics. It is therefore reasonable to suppose that the combined action of Mg-RE texture and rest texture components in fine DRXed grains leads to a random texture, while coarse un-DRXed grains maintain a strong basal texture, exhibiting a heterogeneous texture feature.

4.2. In-situ EBSD mapping and GND characterization

To investigate the deformation mechanism of ER3.9 sample with heterogeneous structure, the in-situ IPF maps of ER12.8 sample with a homogeneous structure and ER3.9 sample were car-

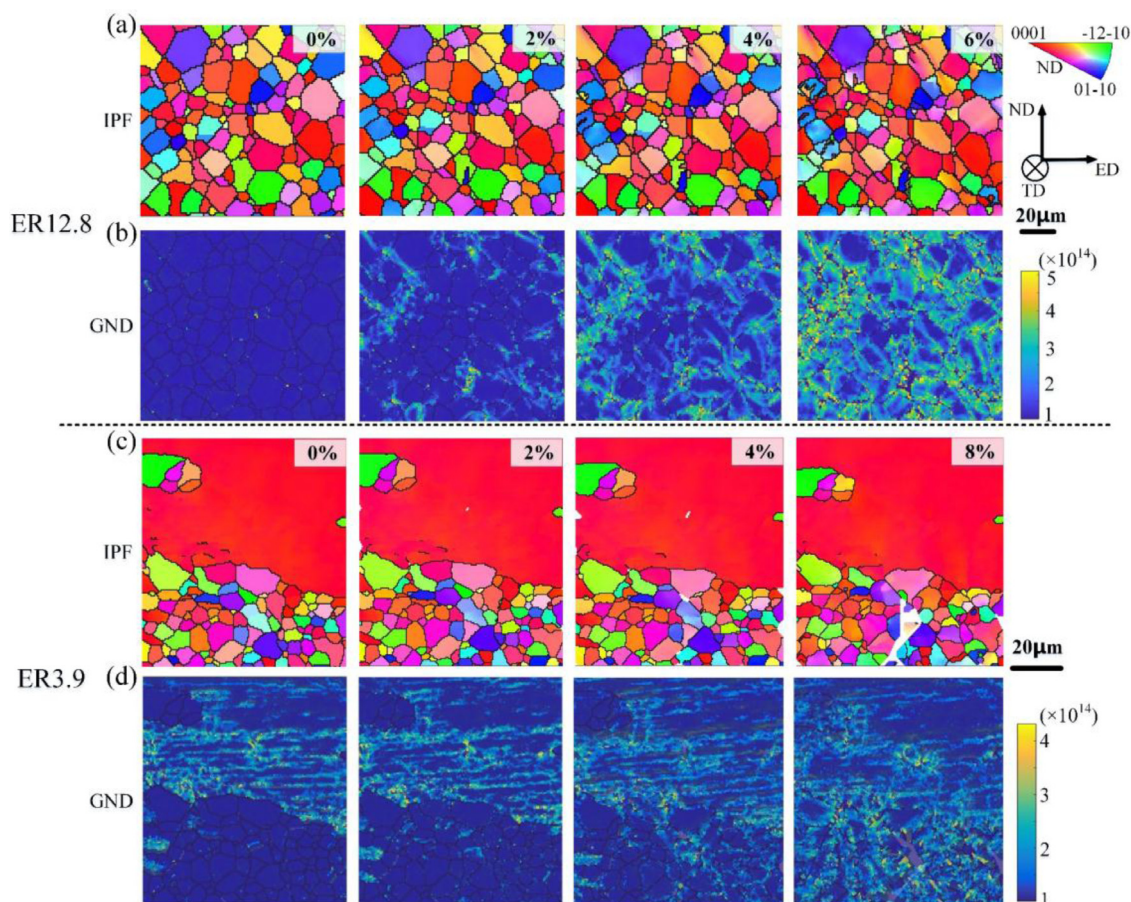


Fig. 8. IPF maps (a) and GND maps (b) of ER12.8 sample at 0%, 2%, 4%, and 6% strains; the IPF maps (c) and GND maps (d) of ER3.9 sample at 0%, 2%, 4%, and 8% strains.

ried out at different strains, respectively (Fig. 8(a, c)). The local region of the ER3.9 sample with heterogeneous texture near domain boundary was selected to study the GND evolution. The GND evolution analysis of ER12.8 and ER3.9 samples is reliable since their indexing rates are more than 85% during the in-situ tensile. The local misorientations are obtained by the kernel average misorientation (KAM) based on the EBSD orientation data [53]. The average local misorientation of a measurement point is calculated by the twenty-four surrounding points at the region of $500 \text{ nm} \times 500 \text{ nm}$, represented by Eq. (3) [8]:

$$\theta = \frac{\sum_{i=1}^{24} \theta_i I_{(\theta_i < \alpha)}}{\sum_{i=1}^{24} I_{(\theta_i < \alpha)}} \quad (3)$$

where θ is the calculated average local misorientation, θ_i represents the misorientation between a measurement point and its neighbor points, and $I_{(\theta_i < \alpha)}$ denotes an indicator function [8]. The values exceeding the predefined threshold of 2° are excluded from the calculation since these points are considered as adjacent grains or subgrains instead of the accumulation of GND [53,54]. Therefore, the GND density ρ_{GND} can be calculated by Eq. (4) proposed by Gao et al. [55] and Kubin et al. [56]:

$$\rho_{\text{GND}} = 2\theta / ub \quad (4)$$

where u and b represent the unit length and the Burger's vector, respectively.

Fig. 8(b, d) shows the calculated GND density maps of ER12.8 and ER3.9 samples by self-developed code based on Eqs. (3, 4). It can be seen that the GNDs distribution in the ER12.8 sample concentrates at the grain boundaries at early deformation. As

the increase of strain, it shows a uniform distribution and the integral level of GND density continuously increases, which can be confirmed by Fig. 9(d). Note that the increasing rate of GND density gradually achieves saturation due to the limited dislocation storage space at late deformation (Fig. 9(e)). As seen from Fig. 8(d), the GND distribution is uneven between coarse and fine grains of the ER3.9 sample, resulting from heterogeneous deformation behavior, which is greatly different from that of the ER12.8 sample. In addition, it accumulates seriously at the near domain boundary and Sub-GBs in coarse grains. With increasing strain, the GNDs distribution has no obvious change in coarse grains but increases significantly in fine grains. Remarkably, as shown in Fig. 9(f), the GND density in coarse grains nearly maintains a level of $1.2 \times 10^{14} / \text{m}^2$ at all strains, while that in fine grains sharply increases and even exceeds the level of coarse grains at later plastic deformation. Moreover, the total increasing rate of GND density of fine grains is significantly higher than that in coarse grains (Fig. 9(g)), especially at early plastic deformation (0%–4%). These results demonstrate that the crystallographic orientation greatly affects the distribution of GND density in addition to the GBs and domain boundaries, which further influences the development of HDI strengthening and hardening [54,57]. The detailed relationship between texture and HDI strengthening and hardening will be discussed in Section 4.5. It should be mentioned here that the GND density in the coarse grains decreases slightly when the strain increases to 2%, which may be because the rate of dislocation annihilation in the DRV process is greater than the rate of dislocation increase, i.e., the rate of work hardening [27].

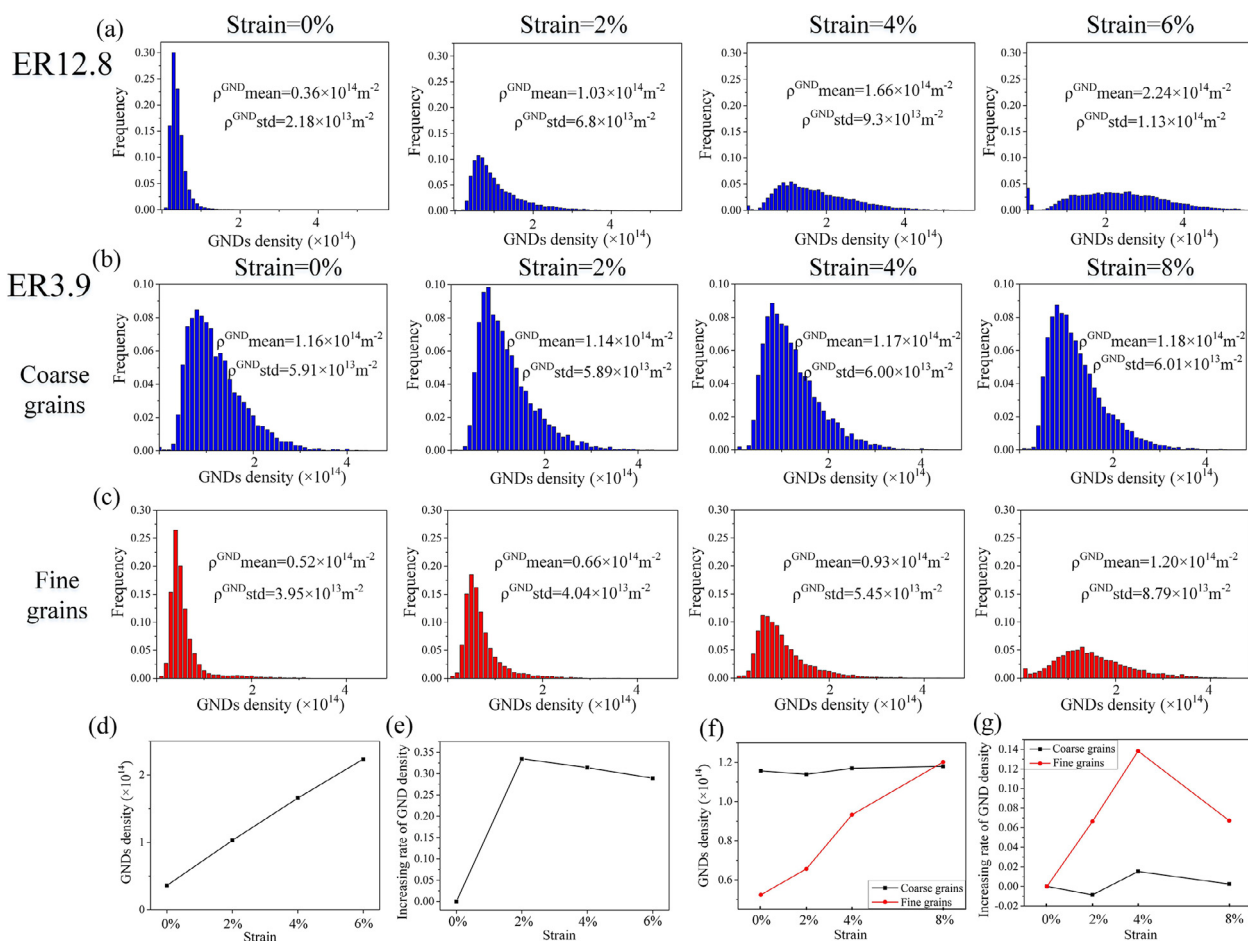


Fig. 9. Histogram distribution of GND density in ER12.8 sample (a), coarse grains (b), and fine grains (c) of ER3.9 sample at different strains; the change of GND density of ER12.8 sample (d) and coarse and fine grains of ER3.9 sample (f) at different strains; the increasing rate of GND density of ER12.8 sample (e) and coarse and fine grains of ER3.9 sample (g) at different strains.

4.3. Mechanism for strength–ductility synergy

4.3.1. Abnormally enhanced strength in coarse grain and improved ductility in fine grain

According to the Hall–Petch law, the YS increases with the decreasing grain size in metal material. If the coarse and fine grains of the ER3.9 sample are equivalent to the AGS, the samples have significant grain refinement from 12.8 μm to 4.6 μm with decreasing extrusion ratios, indeed resulting in the enhancement of YS. Based on Fig. 2(d–f), the interaction between nanoscaled precipitates in three samples and dislocations also facilitates precipitation hardening and alleviates stress concentration, maintaining their large plastic deformation [58,59]. Correspondingly, it also leads to precipitation strengthening. Generally, in heterogeneous materials, the dislocation density in fine grains reaches saturation rapidly with the increase of strain, making the material maintain high strength, while the coarse grains have more space to accommodate the new dislocation generated by plastic deformation, which provides a higher work hardening capacity and makes the material possess high ductility [60]. However, the texture of Mg alloys greatly influences the dislocation behavior of coarse and fine grains and plays a significant role in their strength and ductility.

It was reported that the activity of basal slip is easier than that of prismatic and pyramidal slips due to its lower critical resolved shear stress (CRSS) at room temperature, which depends on the Schmid factor (SF) related to texture [61]. To characterize the change of SF in the ER3.9 sample between coarse and fine grains

during deformation, based on Fig. 10(a, c), the SF distribution histograms for the basal slip of coarse and fine grains was calculated at different strains as shown in Fig. 10(b, d). The texture components of coarse and fine grains exhibit a heterogeneous texture. Besides, there is almost no observable change of texture intensity of whether coarse or fine grains during tensile deformation. On one hand, the *c*-axis of the crystal in coarse grains is nearly parallel to ND, presenting a strong basal texture. The distribution of SF indicates that the coarse grains are always located in the hard orientation and the average SF maintains about 0.1 during deformation (Fig. 10(b)). This makes the activation of basal slip difficult when stretched along ED, exhibiting high deformation resistance and YS [62]. Thus, the hard orientation makes the coarse-grain domains appear stronger. On the other hand, the *c*-axis of crystal in fine grains deflect different angles, exhibiting a random texture component. The average SF retains about 0.31 in fine grains and most of the fine grains are always located in the soft orientation during deformation (Fig. 10(d)), which helps with the activation of basal and non-basal slips.

To evaluate the contribution of various slip modes in accommodating the plastic deformation, the analysis of slip trace was performed in coarse and fine grains. Compared to the TEM characterization for investigating the dislocation features in only a few grains, the slip trace analysis utilized via EBSD combined with SEM focuses on more statistical research of the slip activities in amounts of grains [63]. Based on the Euler angles obtained from EBSD data and self-developed code, the slip trace analysis was per-

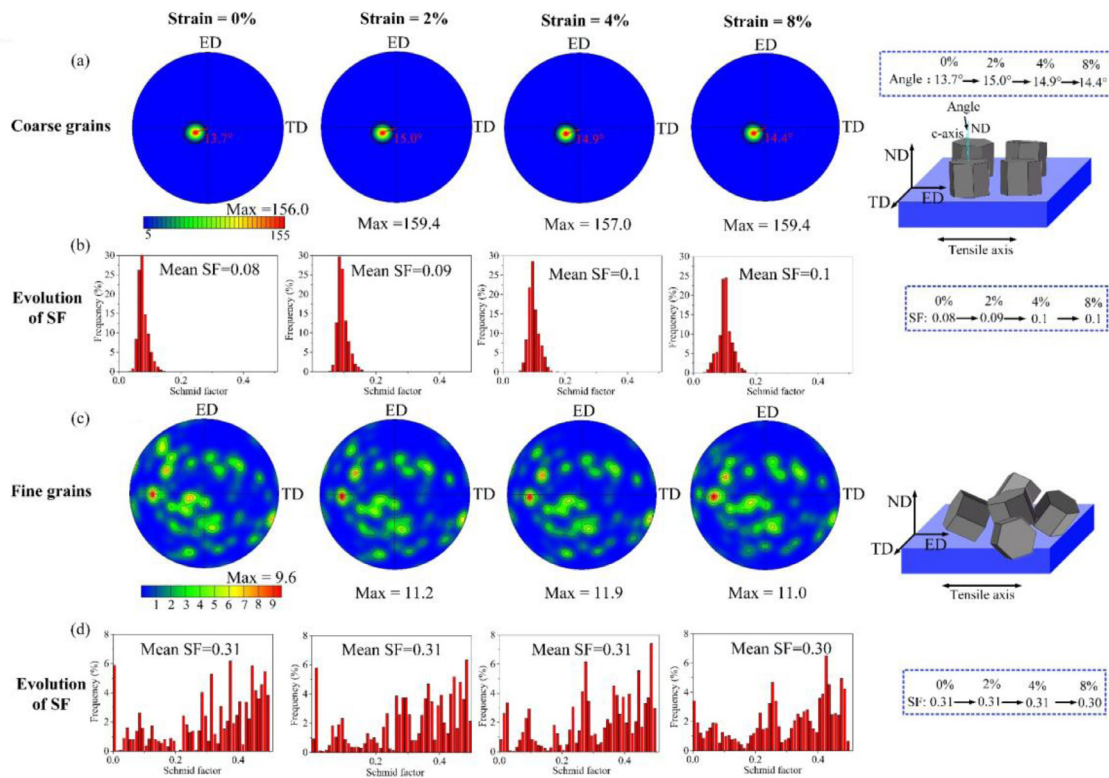


Fig. 10. Evolution of heterogeneous texture between coarse and fine grains and SF distribution histograms of ER3.9 sample under 0%, 2%, 4%, and 8% strains: (a) and (b) coarse grains, (c) and (d) fine grains.

Table 1

Calculated Schmid factors of the twelve slip systems in Grains 222, 326, 329, and 390. SFs of the activated slip system (s) are bolded for each grain.

Slip mode	Slip systems	Slip plane	Slip direction	Schmid factors			
				Grain 222	Grain 326	Grain 329	Grain 390
Basal $\langle a \rangle$ slip	1	(0001)	$[\bar{2}110]$	0.49	0.12	0.44	0.04
	2	(0001)	$[\bar{1}\bar{1}20]$	0.23	0.01	0.04	0.34
	3	(0001)	$[\bar{1}2\bar{1}0]$	0.27	0.13	0.39	0.31
Prismatic $\langle a \rangle$ slip	4	(01 $\bar{1}0$)	$[2\bar{1}\bar{1}0]$	0.03	0.46	0.24	0.08
	5	(10 $\bar{1}0$)	$[\bar{1}2\bar{1}0]$	0.25	0.37	0.30	0.39
	6	($\bar{1}100$)	$[\bar{1}1\bar{2}0]$	0.22	0.10	0.05	0.31
Pyramidal $\langle c + a \rangle$ slip	7	(11 $\bar{2}2$)	$[\bar{1}\bar{1}23]$	0.25	0.01	0.18	0.38
	8	($\bar{1}2\bar{1}2$)	$[\bar{1}2\bar{1}3]$	0.01	0.29	0.21	0.31
	9	($\bar{2}112$)	$[2\bar{1}\bar{1}3]$	0.27	0.23	0.27	0.09
	10	($\bar{1}\bar{1}22$)	$[\bar{1}123]$	0.05	0.001	0.14	0.07
	11	($\bar{1}2\bar{1}2$)	$[\bar{1}2\bar{1}3]$	0.25	0.41	0.15	0.03
	12	($2\bar{1}\bar{1}2$)	$[\bar{2}113]$	0.18	0.33	0.13	0.06

formed to identify the actual slip mode by matching 1452 grains with surface slip (Fig. 11(a)), such as grains 222, 326, 329, and 390 (Fig. 11(b)). Table 1 enumerates some examples to calculate the SFs of 12 slip systems (SS) in selected grains, such as, SS 1–3 for basal $\langle a \rangle$ slip, SS 4–6 for prismatic $\langle a \rangle$ slip, SS 7–12 for pyramidal $\langle c + a \rangle$ slip. For instance, among SS 7–12 of grain 222 with the same slip plane, the $(11\bar{2}2)[\bar{1}\bar{1}23]$ well matches the actual slip lines and has the SF of 0.25 marked by bold font, which is inferred as the activated slip system. Note that the activation of cross slips occurs in grain 390 and the SS of that are identified as the $(\bar{1}100)[11\bar{2}0]$ and $(11\bar{2}2)[\bar{1}\bar{1}23]$. Note if a grain developed more than one slip mode, then each slip mode is counted once.

For coarse grains, the basal and prismatic $\langle a \rangle$ slips are activated, but pyramidal $\langle c + a \rangle$ slip is not detected. For fine grains, the statistical results about the activated number and slip modes are summarized in Table 2. There are 338 activated grains and the

cross slips occur in 29 grains. Based on Table 2, note that the basal $\langle a \rangle$ slip plays a dominant role in the deformation process and the number of them increases with increasing SFs, which presents a typical “Schmid behavior” (Fig. 11(c, d)). The fraction of activated pyramidal $\langle c + a \rangle$ slip is nearly twice that of prismatic $\langle a \rangle$ slip, which accommodates the strain of $\langle c \rangle$ axis in Mg alloys, promoting ductility. This is consistent with the result that various orientations of fine grains with a size less than $5 \mu\text{m}$ contribute to the activation of basal and non-basal slips [64]. The fraction of activated pyramidal $\langle c + a \rangle$ slip may be related to the complex stress state of the interface influence region (IAZ) interface affected zone (IAZ) and the decreasing CRSS due to the addition of rare elements and the decrease of grain size [13,19,65,66]. In addition, a certain proportion of dislocation cross-slip verified by intersecting slip traces was frequently detected between basal and non-basal planes, which benefits for coordinating plastic deformation to retain increasing ductility.

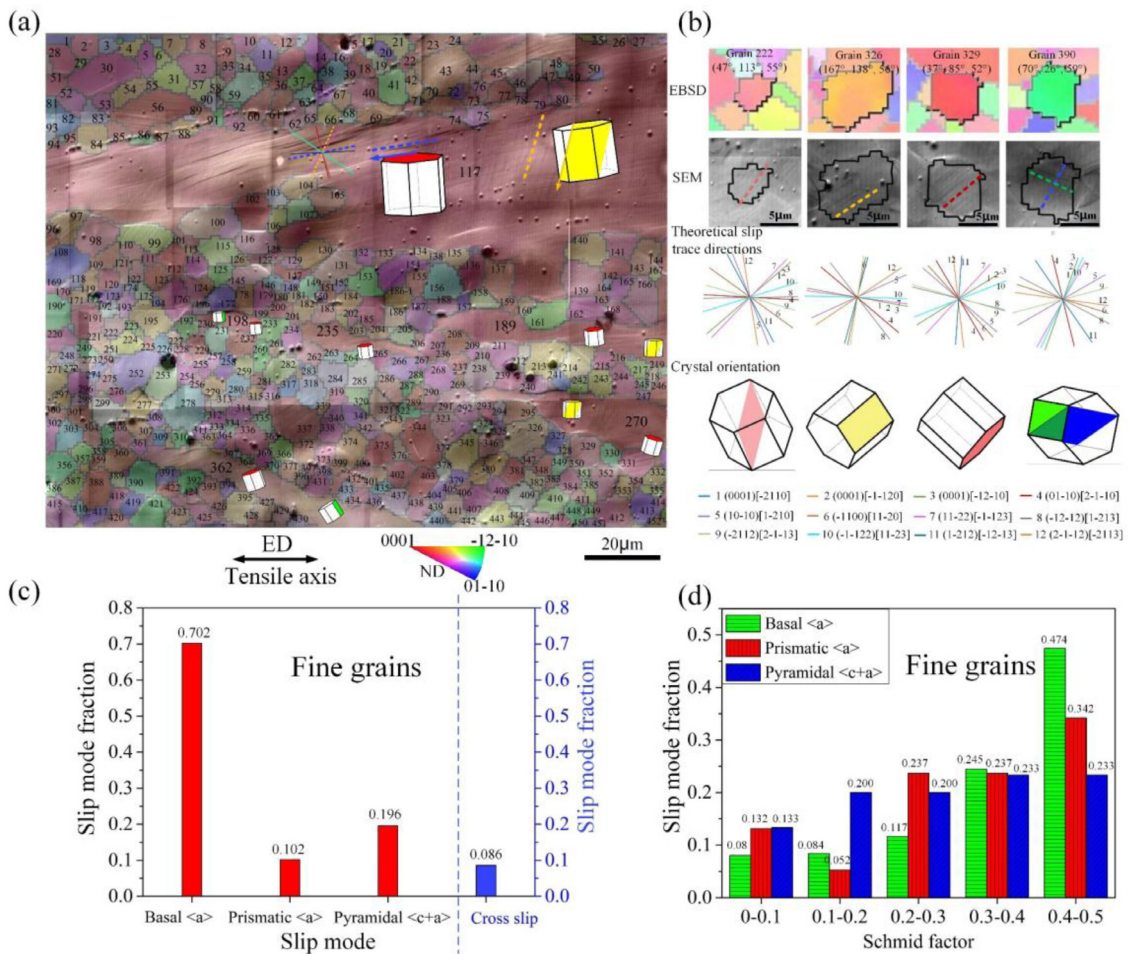


Fig. 11. (a) Superposition of SEM map on IPF map at Mg-13Gd. (b) Slip trace analyses on highlight grains 222, 326, 329, and 390 based on SEM map, EBSD maps, and theoretical slip trace directions after 5% strain. (c) Statistics of the identified slip activity in fine grains with 446 grains of Mg-13Gd sample and (d) corresponding SFs of the activated slip systems after 5% strain.

Table 2
Statistical number and slip modes in fine grains.

Grain (number)	Activated (338)	Non-activated (114)	Cross slip (29)
Slip mode (number)	Basal (a) slip (261)	Prismatic (a) slip (38)	Pyramidal (c + a) slip (73)

The twinning deformation should be considered besides the dislocation mode during the tensile test at room temperature. Fig. 12(a–c) shows the band contrast (BC) maps of three samples at various extrusion ratios after the tensile tests. Note that some {10 $\bar{1}2$ } tensile twins can be observed at three samples and gradually decrease as the decreasing extrusion ratio, while the {10 $\bar{1}1$ } and {10 $\bar{1}3$ } compression twins are rarely detected. The {10 $\bar{1}2$ } tensile twins to coordinate plastic strain can be computed by Eq. (5) [66]:

$$\varepsilon_{\text{twin}} = f_{\text{twin}} \times m \times \gamma_{\text{twin}} \quad (5)$$

where f_{twin} and m represent the volume fraction and the mean SF of tensile twins, respectively. γ_{twin} is the characteristic shear factor (0.13). The calculated $\varepsilon_{\text{twin}}$ of ER12.8, ER6.4, and ER3.9 samples are 0.03%, 0.02%, and 0.02%, respectively. Moreover, as shown in Fig. 12(d), the fraction of low angle grain boundary (0°–5°) is much higher than the 86.3° twin boundary. Therefore, it can be determined that the dislocation slips play a leading role during deformation, while the tensile twins only play an auxiliary role in coordinating deformation to stimulate further slip.

4.3.2. HDI strengthening and hardening

Fig. 13(a) shows the true LUR stress–strain curves of ER12.8, ER6.4, and ER3.9 samples. All samples show hysteresis loops in Fig. 13(b), which indicates that the deformation is uneven among them. Note that the ER12.8 sample with the homogeneous structure still has the inhomogeneous deformation due to the effect of the texture, precipitates, and GBs [67]. Meanwhile, although the ER3.9 sample has a heterogeneous structure and exists more serious inhomogeneous deformation, the ER12.8 and ER6.4 samples have much plump hysteresis loops than that of ER3.9 sample. This is maybe because the strong basal texture in coarse grains deriving from the above analyses plays a significant role in restraining hysteresis loops.

In terms of the relationship between internal stress and dislocation, internal stress can be classified into HDI stress and effective stress [5,68]. The HDI stress is related to the pile-up of GNDs at the interface in soft domains, while the effective stress caused by traditional dislocations (statistical storage dislocations (SSDs)) is the thermal-related isotropic part of internal stress [68,69]. Real-time tracking of the evolution of HDI stress and effective stress would be an operative method to study deformation behavior between

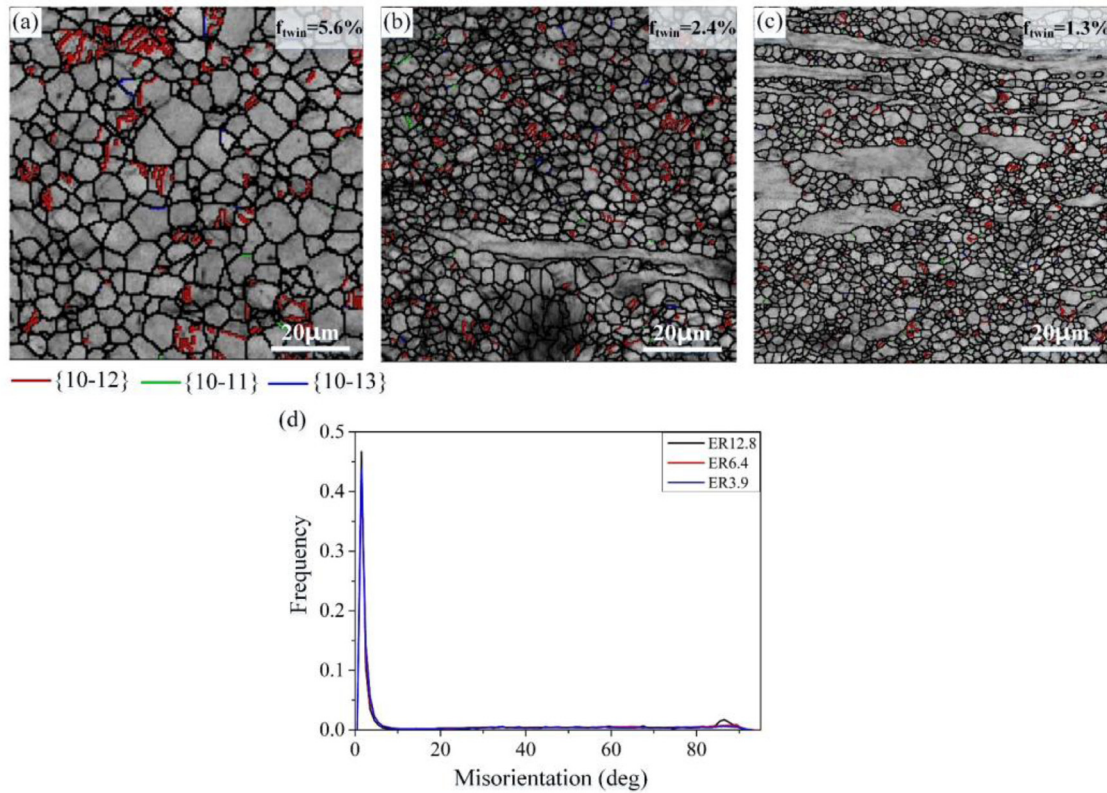


Fig. 12. Band contrast maps of (a) ER12.8, (b) ER6.4, (c) ER3.9 samples; (d) the misorientation map.

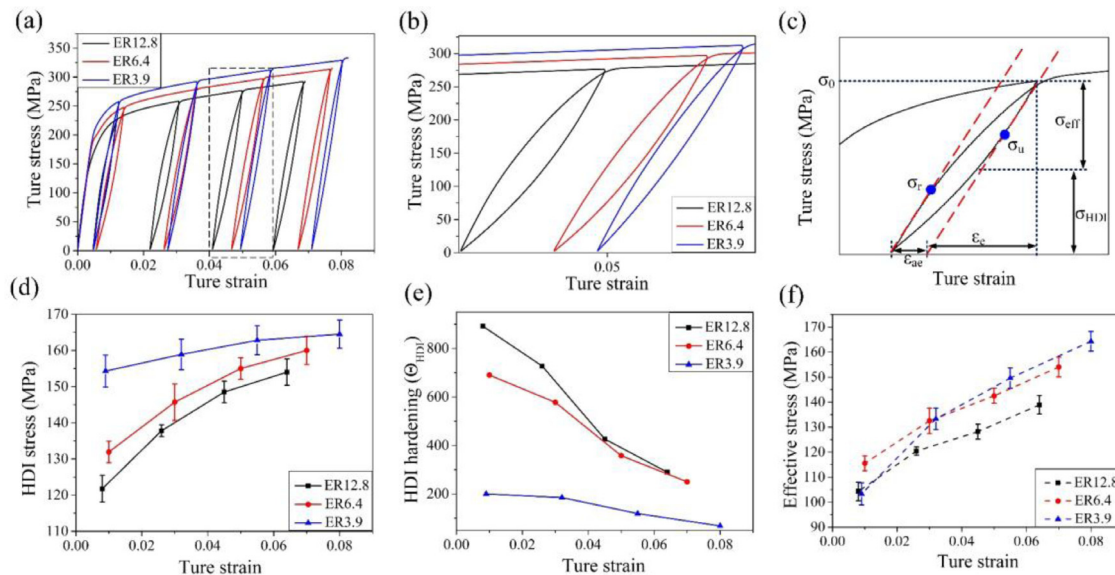


Fig. 13. (a) LUR tensile curves of ER12.8, ER6.4, and ER3.9 samples. (b) Partially enlarged hysteresis loops of different samples. (c) Schematic illustration of the partition of hetero-deformation induced stress (σ_{HDI}) and effective stress (σ_{eff}) in the loading-unloading cycle. The ϵ_{ae} and ϵ_e are represented the anelastic recovery strain and the elastic recovery strain, respectively. The evolution of (d) HDI stress and (e) HDI hardening; (f) the effective stress of different samples with increasing tensile strain.

coarse and fine grains. As shown in Fig. 13(c), the HDI stress σ_{HDI} can be calculated by Eq. (6) proposed by Yang et al. [70] and the σ_{eff} can be obtained by Eq. (7):

$$\sigma_{HDI} = (\sigma_u + \sigma_r)/2 \quad (6)$$

$$\sigma_{eff} = \sigma_0 - \sigma_{HDI} \quad (7)$$

where σ_u and σ_r represent the unloading yield stress and the reloading yield stress, respectively. σ_0 and σ_{eff} are the flow stress

and the effective stress, respectively. To ensure good accuracy, the elastic modulus reduction with 10% was used to measure σ_u and σ_r [71]. In the unloading process, the HDI stress (formerly known as back stress) forces dislocations to move in the opposite direction, generating σ_μ , while the applied stress needs to overcome the frictional stress and HDI stress, resulting in the forward movement of the dislocations during reloading, which generates the σ_r [50]. As seen from Fig. 13(d), although the increasing rate of the HDI stress for the ER3.9 sample is lower than that of ER12.8

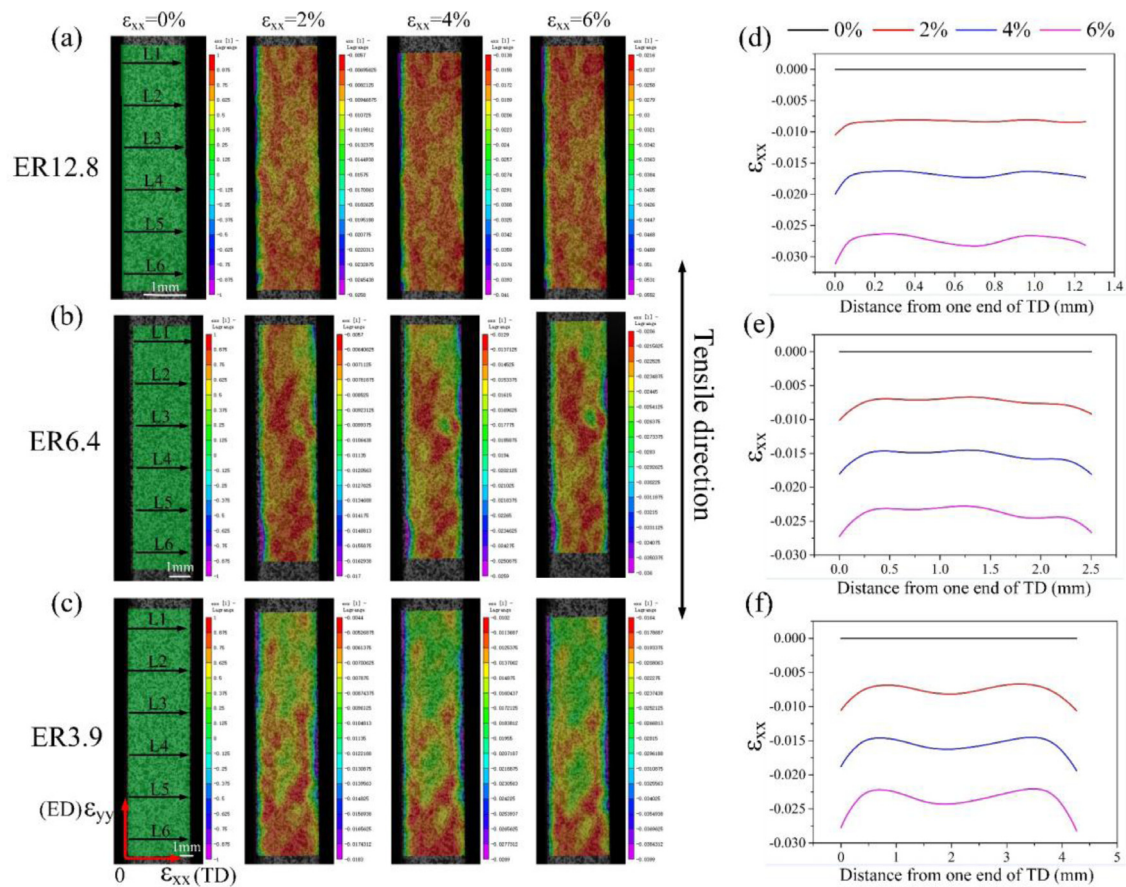


Fig. 14. Macroscopic strain distribution of (a) ER12.8, (b) ER6.4, and (c) ER3.9 samples during tension along ED; (d), (e), and (f) are corresponding average strain distribution curves along the designated paths L1–L6 at different tensile strains.

and ER6.4 samples, overall, the HDI stress of ER3.9 sample is still higher than the ER12.8 and ER6.4 samples. This is mainly because the coarse grains of the ER3.9 sample have more space to accommodate the pile-up of GNDs and produce longer pile-up length near the domain boundaries compared to homogeneous structure, thereby inducing higher HDI stress, which is one of the reasons to enhance the yield strength, i.e., HDI strengthening.

The HDI hardening Θ_{HDI} can be regarded as the slope of the curve in Fig. 13(d), which is defined by Eq. (8) [4]:

$$\Theta_{\text{HDI}} = d\sigma_{\text{HDI}}/d\varepsilon \quad (8)$$

Fig. 13(e) indicates that the Θ_{HDI} of ER12.8 and ER6.4 samples is more remarkable at low applied strains and becomes weaker at large plastic strains, while that of ER3.9 sample is weaker at all strains. This is because the accumulation of GNDs in coarse grains near the domain boundaries is not significantly increased during the plastic deformation due to its strong basal texture (Fig. 10(a)). Meanwhile, the low stacking fault energy (SFE) in Mg-RE alloys can cause dislocation to be pushed into domain boundaries, and the occurrence of cross slip in coarse grains, as shown in Fig. 11(c), also influences the accumulation of GNDs to some extent [72]. These results weaken the HDI hardening effect in the ER3.9 sample.

Note that the effective stress of the ER3.9 sample increases rapidly at the later deformation and exceeds that of ER12.8 and ER6.4 samples (Fig. 13(f)). Based on the above analyses, the fine grains of the ER3.9 sample help with the nucleation and entanglement of dislocations at large strain compared with coarse grains. Moreover, the high HDI stress also promotes the activation of more slip systems near the domain boundaries. These intertwined factors make the effective stress sharply increase [68,69,73]. There-

fore, compared with the HDI hardening of ER3.9 samples, the traditional dislocation hardening mainly caused by fine grains plays a dominant role in overall strain hardening.

4.4. Macroscopic and microscopic strain distribution based on DIC technology

The DIC technology proposed by Peter and Ranson [74] was used to characterize the strain distribution of two or three dimensions, which can effectively study the deformation behavior of materials. To compare the difference of total strain at three samples, the LR-DIC analysis was performed. It can be seen in Fig. 14(a, b) that the ER12.8 and ER6.4 samples exhibit a uniform strain distribution during tensile deformation and the total strain gradually increases with increasing strains, reflecting the principle of iso-strain. While the ER3.9 sample has a remarkable gradient change trend (Fig. 14(c)). This is also confirmed by the quantitative analysis of average strain ε_{xx} obtained by the designated paths L1–L6 at different tensile strains, as shown in Fig. 14(d–f). Thus, combined with Section 3.1, the strain distribution depends on the difference of microstructure and texture among the three samples.

To further investigate the evolution of the local strain of the ER3.9 sample with HLS and heterogeneous texture, the HR-DIC analysis was carried out to study the detailed deformation behavior of the ER3.9 sample based on the change of speck markers in SEM images during tensile deformation. Up to now, lots of literature have studied the deformation behavior of materials at a small scale via HR-DIC, such as the strain distribution of lath martensite [75], twinning behavior of TiAl lamellar structure [76], and the effect of interface on mechanical properties of layered Cu/Cu-10 Zn

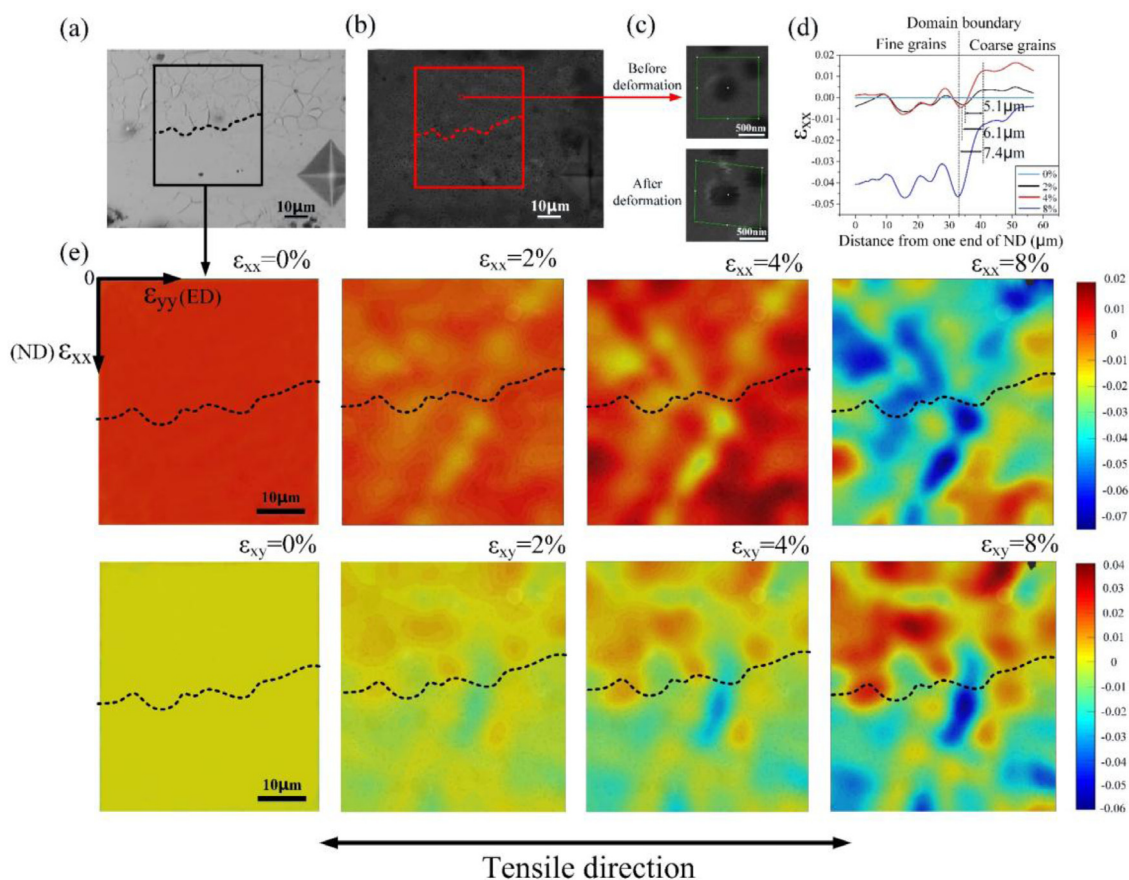


Fig. 15. (a) Optical micrographs of the selected region including coarse and fine grains marked by the black rectangle; (b) SEM images of speck markers used for DIC; (c) detailed distribution of the speck markers before and after deformation; (d) average strain distribution curves along ND; (e) microscopic strain (ε_{xx} and ε_{xy}) distribution in ER3.9 samples at different strains during tension along ED.

composites [69], etc. Fig. 15(a) shows the optical micrographs of the selected region with coarse and fine grains marked by black rectangle so that we can directly distinguish the strain distribution of coarse and fine grains. The speck markers with nanoscale can be identified before and after deformation as shown in Fig. 15(b, c).

As shown in Fig. 15(e), the ε_{xx} strain localization has appeared under a low macroscopic strain with 2% and then is exaggerated with increasing macroscopic strains. It is worth noting that the serious compressive strain distributes in coarse and fine grains. The coarse grains still possess a lot of low strain regions at 8% macroscopic strain. This is because the plastic deformation of coarse grains with a strong basal texture is difficult, which is also supported by the change of GND density of coarse grains. Meanwhile, the ε_{xx} and ε_{xy} distribution reveal that fine grains bear higher strain levels and extend into the coarse grains, releasing strain localization. This is because of the constraint effect by the surrounding coarse grains with hard orientation during deformation.

Fig. 15(d) quantitatively analyzes the results of strain cloud image at different strains. It indicates that the strain distribution of fine grains occurs with apparent fluctuation, while the coarse grains present a uniform strain distribution with a lower strain level. Interestingly, a significant strain gradient appears near the domain boundary between coarse and fine grains and it gradually increases with increasing macroscopic strains. This strain gradient should be directly caused by the deformation difference of coarse and fine grains, where fine grains with a random texture that are readily compatible with plastic deformation and the coarse grains with strong basal texture are difficult to deform with increasing strains. Generally, the distance from maximum strain to minimum

strain in coarse or fine grains is defined as IAZ, which is produced in the zone with strain gradient due to the pile-up of GNDs at the interface in the soft domain [69,77,78]. Thus, the width of IAZ also gradually increases from 5.1 μm to 7.4 μm with increasing macroscopic strains as shown in Fig. 15(d), which is different from the layered Cu/Cu-10 Zn composites with the constant IAZ [8]. This may be influenced by texture and the HLS without layered interface in Mg alloys, such as types of the texture and the size of coarse grains along ND or ED in HLS, etc.

4.5. Role of heterogeneous texture on coarse and fine grains during deformation

During plastic deformation of heterogeneous structure materials, the GNDs accumulating at the interface in the coarse grain zones contribute to the development of HDI stress, resulting in high strength. Meanwhile, the strain partition in coarse grain zones at larger tensile strain induces the increase of strain gradient, which needs more GNDs to accommodate it, inducing additional strain hardening (i.e., HDI hardening), which facilitates retaining ductility [67]. Therefore, the effect of HDI strengthening and hardening depends on the GND density at the domain boundary. For the ER3.9 sample, the most prominent microstructural parameter is heterogeneous texture as well as HLS. The role of heterogeneous texture on HDI strengthening and hardening during deformation has been not studied so far. For instance, Ma et al. [8] fabricated the copper/bronze laminates by accumulative roll bonding (ARB) processing and post-annealing and studied the effect of domain interface on HDI stress. Li et al. [13] designed alternating coarse-

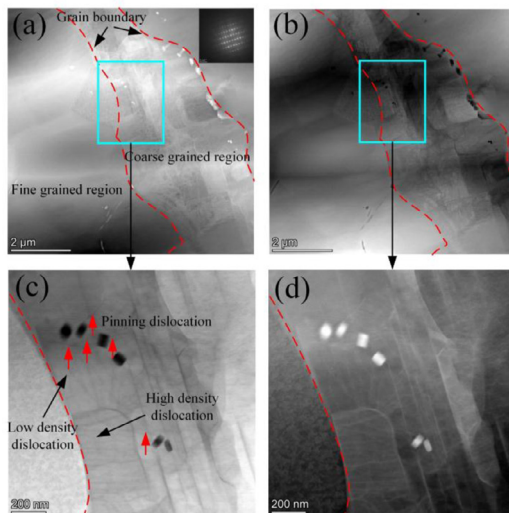


Fig. 16. TEM images of ER3.9 sample after 2% strain: (a) annular bright-field (ABF) image and (b) high-angle annular dark-field (HAADF) image of the microstructure in DRXed and un-DRXed regions; (c) and (d) are the corresponding magnification images, respectively.

and fine-grain layers of pure Ti and the deformation mechanism at interface between coarse- and fine-grain layers was investigated. However, the influence of interfacial texture was not considered among the factors studied in these researches.

In our HLS binary Mg-13Gd, the coarse grains with strong basal texture are always located in the hard orientation during deformation, which makes the basal slip activity difficult and is not conducive to increasing GND density near domain boundary, weakening the HDI hardening effect. In addition, the occurrence of cross slip and low SFE in the sample is also not conducive to the accumulation of GNDs to some extent based on the discussion in Section 4.3.2. Fig. 16 shows annular bright-field (ABF) and corresponding high-angle annular dark-field (HAADF) images of ER3.9 sample with an electron beam parallel to $[11\bar{2}0]_{\alpha-Mg}$ after 2% strain. The dynamic precipitates with a mean size of 127 nm are mainly distributed in the coarse grains, where the profuse substructures also form. Note that some dislocations are pinned by precipitates marked by red arrows (Fig. 16(c)), leading to dislocation entanglement and increasing dislocation density near precipitates inside coarse grains. However, this prevents the dislocation from moving towards the coarse grain boundary, resulting in a lower dislocation density at the coarse grain boundary, which further reduces the HDI hardening effect. Meanwhile, the deformation behavior of precipitates also in turn leads to the precipitation strengthening. Nevertheless, the longer pile-up length of partial GNDs at domain interface in coarse grains due to their enough space for dislocation storage leads to a higher level of HDI stress and promotes the HDI strengthening as shown in Figs. 13(d) and 16. The traditional dislocation hardening mainly caused by fine grains with the random texture plays a dominant role in overall strain hardening, which is consistent with the results of higher strain levels in fine grains obtained by digital image correlation. Moreover, the activation of non-basal slips, especially pyramidal $\langle c + a \rangle$ slip, and cross slips in fine grains benefit for coordinating plastic deformation.

Furthermore, it is hypothesized that there exists an optimal texture component to affect HDI strengthening and hardening in heterogeneous structure Mg alloys. Compared to the strong basal or fiber texture, the basal split texture shows great potential in activating basal or non-basal slip [62,79]. Therefore, how to optimize

the design of texture components of coarse and fine grains still needs further research.

5. Conclusions

In this work, binary Mg-13Gd alloy with the HLS and heterogeneous texture was successfully prepared by a small extrusion ratio. The evolution of microstructure and texture, the development of mechanical properties, and the effect of the heterogeneous texture on the deformation behavior of heterogeneous Mg-13Gd alloy were systematically studied. Several mainly conclusions can be drawn as follows:

- (1) The ER3.9 sample presented a dramatic HLS and heterogeneous texture resulting from the DDRX, where the fine DRXed grains formed a random texture and coarse un-DRXed maintained a strong basal texture.
- (2) The ER3.9 sample showed an extraordinary combination of strength–ductility compared to ER12.8 and ER6.4 samples with a homogeneous structure. The enhanced strength is mainly attributed to the texture strengthening in coarse grains and HDI strengthening besides precipitation strengthening and grain refinement. The improving ductility is mainly due to the weakened texture in fine grains.
- (3) In coarse grains, the strong basal texture, the occurrence of cross slip, low SFE, and dislocation pinned by precipitates weakened the HDI hardening effect. While the traditional dislocation hardening mainly generated by fine grains dominated overall strain hardening. Meanwhile, the activation of non-basal slips, especially pyramidal $\langle c + a \rangle$ slip, and the generation of cross slips in fine grains benefited for coordinating plastic deformation.
- (4) The ability for coordinate plastic deformation in fine grains was higher than that of coarse grains due to the heterogeneous texture, which is confirmed by the LR-DIC and HR-DIC technologies.

Acknowledgment

This work was financially supported by the National Natural Science Foundation of China (Nos. 52071035 and U1764253).

References

- [1] M.X. Yang, F.P. Yuan, Q.G. Xie, Y.D. Wang, E. Ma, X.L. Wu, *Acta Mater.* 109 (2016) 213–222.
- [2] X.L. Wu, M.X. Yang, F.P. Yuan, G.L. Wu, Y.J. Wei, X.X. Huang, Y.T. Zhu, *Proc. Natl. Acad. Sci.* 112 (2015) 14501–14505.
- [3] X.L. Wu, Y.T. Zhu, *Mater. Res. Lett.* 5 (2017) 527–532.
- [4] X.T. Fang, G.Z. He, C. Zheng, X.L. Ma, D. Kaoumi, Y.S. Li, Y.T. Zhu, *Acta Mater.* 186 (2020) 644–655.
- [5] Y.T. Zhu, X.L. Wu, *Mater. Res. Lett.* 7 (2019) 393–398.
- [6] J.F. Song, J. She, D.L. Chen, F.S. Pan, *J. Magnes. Alloy* 8 (2020) 1–41.
- [7] Y. Yang, X.M. Xiong, J. Chen, X.D. Peng, D.L. Chen, F.S. Pan, *J. Magnes. Alloy* 9 (2021) 705–747.
- [8] X. Ma, C. Huang, J. Moering, M. Ruppert, H.W. Höppel, M. Göken, J. Narayan, *Acta Mater.* 116 (2016) 43–52.
- [9] Z. Zhang, S.K. Vajpai, D. Orlov, K. Ameyama, *Mater. Sci. Eng. A* 598 (2014) 106–113.
- [10] J. Moering, X.L. Ma, J. Malkin, M.X. Yang, Y.T. Zhu, S. Mathaudhu, *Scr. Mater.* 122 (2016) 106–109.
- [11] K.S. Raju, V.S. Sarma, A. Kauffmann, Z. Hegedus, J. Gubicza, M. Peterlechner, J. Freudenberger, G. Wilde, *Acta Mater.* 61 (2013) 228–238.
- [12] R.G. Li, H.R. Li, H.C. Pan, D.S. Xie, J.H. Zhang, D.Q. Fang, Y.Q. Dai, D.Y. Zhao, H. Zhang, *Scr. Mater.* 193 (2021) 142–146.
- [13] D. Li, G. Fan, X. Huang, D. Juul Jensen, K. Miao, C. Xu, L. Geng, Y. Zhang, T. Yu, *Acta Mater.* 206 (2021) 116627.
- [14] M.Z. Quadir, O. Al-Buhamad, L. Bassman, M. Ferry, *Acta Mater.* 55 (2007) 5438–5448.
- [15] S.H. Park, S.H. Kim, Y.M. Kim, B.S. You, *J. Alloy. Compd.* 646 (2015) 932–936.
- [16] T.H. Fang, W.L. Li, N.R. Tao, K. Lu, *Science* 331 (2011) 1587–1590.
- [17] W. Xu, X.C. Liu, K. Lu, *Acta Mater.* 152 (2018) 138–147.
- [18] N. Stanford, D. Atwell, M.R. Barnett, *Acta Mater.* 58 (2010) 6773–6783.
- [19] S.H. Kim, J.G. Jung, B.S. You, S.H. Park, *J. Alloy. Compd.* 695 (2017) 344–350.

- [20] D. Xia, G. Huang, Q. Deng, B. Jiang, S. Liu, F. Pan, *Mater. Sci. Eng. A* 715 (2018) 379–388.
- [21] A. Styczynski, C. Hartig, J. Bohlen, D. Letzig, *Scr. Mater.* 50 (2004) 943–947.
- [22] Q. Luo, Y.L. Guo, B. Liu, Y.J. Feng, J.Y. Zhang, Q. Li, K. Chou, *J. Mater. Sci. Technol.* 44 (2020) 171–190.
- [23] Y.L. Guo, B. Liu, W. Xie, Q. Luo, Q. Li, *Scr. Mater.* 193 (2021) 127–131.
- [24] X.J. Wang, X.M. Wang, X.S. Hu, K. Wu, *J. Magnes. Alloy* 8 (2020) 421–430.
- [25] K. Yamada, H. Hoshikawa, S. Maki, T. Ozaki, Y. Kuroki, S. Kamado, Y. Kojima, *Scr. Mater.* 61 (2009) 636–639.
- [26] T. Homma, N. Kunito, S. Kamado, *Scr. Mater.* 61 (2009) 644–647.
- [27] I.A. Anyanwu, S. Kamado, Y. Kojima, *Mater. Trans.* 42 (2001) 1206–1211.
- [28] T. Honma, T. Ohkubo, S. Kamado, K. Hono, *Acta Mater.* 55 (2007) 4137–4150.
- [29] K. Yamada, Y. Okubo, M. Shiono, H. Watanabe, S. Kamado, Y. Kojima, *Mater. Trans.* 47 (2006) 1066–1070.
- [30] K.Y. Zheng, J. Dong, X.Q. Zeng, W.J. Ding, *Mater. Sci. Eng. A* 489 (2008) 44–54.
- [31] R. Li, J. Nie, G. Huang, Y. Xin, Q. Liu, *Scr. Mater.* 64 (2011) 950–953.
- [32] K. Wang, J. Wang, S. Huang, S. Gao, S. Guo, S. Liu, X. Chen, F. Pan, *Mater. Sci. Eng. A* 733 (2018) 267–275.
- [33] M. Yamasaki, T. Anan, S. Yoshimoto, Y. Kawamura, *Scr. Mater.* 53 (2005) 799–803.
- [34] Z. Yu, Y. Huang, X. Qiu, G. Wang, F. Meng, N. Hort, J. Meng, *Mater. Sci. Eng. A* 622 (2015) 121–130.
- [35] Z. Zhang, X. Liu, Z. Wang, Q. Le, W. Hu, L. Bao, J. Cui, *Mater. Des.* 88 (2015) 915–923.
- [36] Z. Ma, G. Li, Q. Peng, X. Peng, D. Chen, H. Zhang, Y. Yang, G. Wei, W. Xie, *J. Magnes. Alloy* 10 (2022) 119–128.
- [37] L. Zhang, Z. Chen, Y.H. Wang, G.Q. Ma, T.L. Huang, G.L. Wu, D.J. Jensen, *Scr. Mater.* 141 (2017) 111–114.
- [38] P.J. Shi, Y. Zhong, Y. Li, W.L. Ren, T.X. Zheng, Z. Shen, B. Yang, J.C. Peng, P.F. Hu, Y. Zhang, P.K. Liaw, Y.T. Zhu, *Mater. Today* 41 (2020) 62–71.
- [39] X.L. Ma, C.X. Huang, W.Z. Xu, H. Zhou, X.L. Wu, Y.T. Zhu, *Scr. Mater.* 103 (2015) 57–60.
- [40] S.S. Liu, J.L. Zhang, X. Chen, G.S. Huang, D.B. Xia, A.T. Tang, Y.T. Zhu, B. Jiang, F.S. Pan, *Mater. Sci. Eng. A* 785 (2020) 139324.
- [41] Y.Z. Meng, J.M. Yu, G.S. Zhang, Y.J. Wu, Z.M. Zhang, Z. Shi, *J. Magnes. Alloy* 8 (2020) 1228–1237.
- [42] J. Luo, W.W. Hu, Q.Q. Jin, H. Yan, R.S. Chen, *Scr. Mater.* 127 (2017) 146–150.
- [43] X.B. Zheng, W.B. Du, K. Liu, Z.H. Wang, S.B. Li, *J. Magnes. Alloy* 4 (2016) 135–139.
- [44] A.M. Wusatowska-Sarneck, H. Miura, T. Sakai, *Mater. Sci. Eng. A* 323 (2002) 177–186.
- [45] K. Huang, R.E. Loge, *Mater. Des.* 111 (2016) 548–574.
- [46] B. Dong, X. Che, Z. Zhang, J. Yu, M. Meng, *J. Alloys Compd.* 853 (2021) 157066.
- [47] H. Zhang, H.Y. Wang, J.G. Wang, J. Rong, M. Zha, C. Wang, P.K. Ma, Q.C. Jiang, *J. Alloy. Compd.* 780 (2019) 312–317.
- [48] M. Zha, Y. Li, R.H. Mathiesen, R. Bjørge, H.J. Roven, *Acta Mater.* 84 (2015) 42–54.
- [49] W. Roberts, B. Ahlstrom, *Acta Metall.* 26 (1978) 801–813.
- [50] H. Miura, T. Sakai, S. Andiarwanto, J.J. Jonas, *Philos. Mag.* 85 (2005) 2653–2669.
- [51] H. Miura, T. Sakai, H. Hamaji, J.J. Jonas, *Scr. Mater.* 50 (2004) 65–69.
- [52] H.Y. Wang, Z.P. Yu, L. Zhang, C.G. Liu, M. Zha, C. Wang, Q.C. Jiang, *Sci. Rep.* 5 (2015) 17100.
- [53] M. Calcagnotto, D. Ponge, E. Demir, D. Raabe, *Mater. Sci. Eng. A* 527 (2010) 2738–2746.
- [54] A. Khosravani, D.T. Fullwood, B.L. Adams, T.M. Rampton, M.P. Miles, R.K. Mishra, *Acta Mater.* 100 (2015) 202–214.
- [55] H. Gao, Y. Huang, W.D. Nix, J.W. Hutchinson, *J. Mech. Phys. Solid.* 47 (1999) 1239–1263.
- [56] L.P. Kubin, A. Mortensen, *Scr. Mater.* 48 (2003) 119–125.
- [57] J. Jiang, T.B. Britton, A.J. Wilkinson, *Acta Mater.* 61 (2013) 7227–7239.
- [58] M.S. Mehranpour, A. Heydarinia, M. Emamy, H. Mirzadeh, A. Koushki, R. Razi, *Mater. Sci. Eng. A* 802 (2021) 140667.
- [59] S.S. Liu, W.Z. Wang, X. Chen, G.S. Huang, H. Liu, A.T. Tang, B. Jiang, F.S. Pan, *Mater. Sci. Eng. A* 812 (2021) 141094.
- [60] M. Naseri, M. Reihanian, E. Borhani, *Mater. Sci. Eng. A* 656 (2016) 12–20.
- [61] A. Kula, X. Jia, R.K. Mishra, M. Niewczasz, *Int. J. Plast.* 92 (2017) 96–121.
- [62] G. Wang, G. Huang, X. Chen, Q. Deng, A. Tang, B. Jiang, F. Pan, *Mater. Sci. Eng. A* 705 (2017) 46–54.
- [63] G.M. Zhu, L.Y. Wang, H. Zhou, J.H. Wang, Y. Shen, P. Tu, H. Zhu, W. Liu, P.P. Jin, X.Q. Zeng, *Int. J. Plast.* 120 (2019) 164–179.
- [64] J. Koike, T. Kobayashi, T. Mukai, H. Watanabe, M. Suzuki, K. Maruyama, K. Higashi, *Acta Mater.* 51 (2003) 2055–2065.
- [65] J. Bohlen, M.R. Nurnberg, J.W. Senn, D. Letzig, S.R. Agnew, *Acta Mater.* 55 (2007) 2101–2112.
- [66] B. Song, Q. Yang, T. Zhou, L. Chai, N. Guo, T. Liu, S. Guo, R. Xin, *J. Mater. Sci. Technol.* 35 (2019) 2269–2282.
- [67] Y.F. Liu, Y. Cao, Q.Z. Mao, H. Zhou, Y.H. Zhao, W. Jiang, Y. Liu, J.T. Wang, Z.S. You, Y.T. Zhu, *Acta Mater.* 189 (2020) 129–144.
- [68] Y.F. Wang, M.X. Yang, X.L. Ma, M.S. Wang, K. Yin, A.H. Huang, C.X. Huang, *Mater. Sci. Eng. A* 727 (2018) 113–118.
- [69] C.X. Huang, Y.F. Wang, X.L. Ma, S. Yin, H.W. Hoppel, M. Goken, X.L. Wu, H.J. Gao, Y.T. Zhu, *Mater. Today* 21 (2018) 713–719.
- [70] M. Yang, Y. Pan, F. Yuan, Y. Zhu, X. Wu, *Mater. Res. Lett.* 4 (2016) 145–151.
- [71] L.S. Toth, C.F. Gu, B. Beausir, J.J. Fundenberger, M. Hoffman, *Acta Mater.* 117 (2016) 35–42.
- [72] I.A. Ovid'ko, R.Z. Valiev, Y.T. Zhu, *Prog. Mater. Sci.* 94 (2018) 462–540.
- [73] M.F. Ashby, *Philos. Mag.* 21 (1970) 399–424.
- [74] W.H. Peters, W.F. Ranson, *Opt. Eng.* 21 (1982) 427–431.
- [75] C. Du, J.P.M. Hoefnagels, R. Vaes, M.G.D. Geers, *Scr. Mater.* 120 (2016) 37–40.
- [76] T.E.J. Edwards, F. Di Gioacchino, R. Munoz-Moreno, W.J. Clegg, *Scr. Mater.* 118 (2016) 46–50.
- [77] Y.F. Wang, C.X. Huang, X.T. Fang, H.W. Höppel, M. Göken, Y.T. Zhu, *Scr. Mater.* 174 (2020) 19–23.
- [78] W. Chen, W. He, Z. Chen, B. Jiang, Q. Liu, *Int. J. Plast.* 133 (2020) 102806.
- [79] A. Imandoust, C.D. Barrett, A.L. Oppedal, W.R. Whittington, Y. Paudel, H. El Kadiri, *Acta Mater.* 138 (2017) 27–41.